On the clouds and ammonia in Jupiter's upper troposphere from Juno JIRAM reflectivity observations

Davide Grassi[1,*], A. Mura[1], G. Sindoni[2], A. Adriani[1], S. K. Atreya[3], G. Filacchione[1], L. N. Fletcher[4], J. I. Lunine[5], M. L. Moriconi[6], R. Noschese[1], G. S. Orton[7], C. Plainaki[2], R. Sordini[1], F. Tosi[1], D. Turrini[1], A. Olivieri[2], G. Eichstädt[8], C. J. Hansen[9], H. Melin[4], F. Altieri[1], A. Cicchetti[1], B. M. Dinelli[6], A. Migliorini[1], G. Piccioni[1], S. Stefani[1], S. J. Bolton[10]

(1) Istituto di Astrofisica e Planetologia Spaziali, Istituto Nazionale di Astrofisica, Via del Fosso del Cavaliere, snc, 00133, Roma, Italy

(2) Agenzia Spaziale Italiana, Via del Politecnico, snc, 00133, Roma, Italy

(3) Department of Climate and Space Sciences and Engineering, Univ. of Michigan, 2455 Hayward St, Ann Arbor, MI 48109

(4) School of Physics and Astronomy, University of Leicester, University Rd, Leicester LE1 7RH, UK

(5) Cornell Center for Astrophysics and Planetary Science, Cornell University, 122 Sciences Dr, Ithaca, NY 14853, USA

(6) Istituto delle Scienze atmosferiche e del Clima, Consiglio Nazionale delle Ricerche, Via P. Gobetti 101, 40129, Bologna, Italy

(7) Jet Propulsion Laboratory, California Institute of Technology, 4800 Oak Grove Dr, Pasadena, CA 91109, USA

(8) Independent Scholar, Stuttgart, Germany

(9) Planetary Science Institute, 1700 E Fort Lowell Rd STE 106, Tucson, AZ 85719, USA

(10) Southwest Research Institute, 6220 Culebra Rd, San Antonio, TX 78238, USA

* corresponding author: davide.grassi@inaf.it

Abstract

We analyse spectra measured by the Jovian Infrared Auroral Mapper (JIRAM, a payload element of the NASA Juno mission) in the 3150-4910 cm^{-1} (2.0-3.2 μm) range during the perijiove passage of August 2016. Despite modelling uncertainties, the quality and the relative uniformity of the dataset allow us to determine several parameters characterizing the Jupiter's upper troposphere in the latitude range 35°S-30°N.

Ammonia relative humidity at 500 millibars varies between 5 per cent to supersaturation beyond 100 per cent for about 3 per cent of the processed spectra. Ammonia appears depleted over belts and relatively enhanced over zones. Local variations of ammonia, arguably associated with local dynamics, are found to occur in several locations on the planet (Oval BA, South Equatorial Belt).

Cloud altitude, defined as the level where aerosol opacity reaches unit value at 3650 cm^{-1} (2.74 μm), is maximum over the Great Red Spot (>20 km above the 1 bar level) and the zones (15 km) while it decreases over the belts and toward higher latitudes. The aerosol opacity scale height suggests more compact clouds over zones and more diffuse clouds over belts. The integrated opacity of clouds above the 1.3-bar pressure level is found to be minimum in regions where thermal emission of the deeper atmosphere is maximum. The opacity of tropospheric haze above the 200-mbar level also increases over zones.

Our results are consistent with a Hadley-type circulation scheme previously proposed in literature for belts and zones, with clear hemisphere asymmetries in cloud and haze.

Keywords:

planets and satellites: atmospheres, techniques: spectroscopic, planets and satellites: individual: Jupiter

1. Introduction

The spectrum of Jupiter at wavenumbers ν > 3150 cm^{-1} (λ < 3.17 μm) is dominated by the scattering of solar radiation by aerosols (Taylor et al. 2004). Photons measured by an observer have been subjected to both scattering by particles and absorption by particles and atmospheric gases as they travel through the atmosphere from top, to the reflecting layers, and back again. In Jupiter's atmosphere several gases, including methane, molecular hydrogen, ammonia and, to a lesser extent, phosphine, create absorption features in the spectrum of reflected sunlight. Indeed, the variability of the total gas opacity with wavenumber allows the probing of different altitudes, since solar photons can reach deeper levels in more transparent (i.e., lower opacity) regions of the spectrum. Information on the structure of Jupiter's clouds comes from a variety of techniques, including imaging, spectroscopy, polarimetry and in situ measurements (see West et al. 2004 for a comprehensive review). In most circumstances, the clouds sensed by reflected sunlight are located at pressures p < 2 bar (Fig. 1 in Sromovsky & Fry, 2010a) and are associated with the condensation of ammonia (NH_3) in the upper troposphere, either directly or bound to hydrogen sulfide, as ammonium hydrosulfide (NH_4SH) (Atreya et al. 1999; Baines et al. 2002). In limited spatial regions, where upper clouds are absent, the presence of deeper clouds (p> 4 bar) associated with the condensation of water was inferred from visible imaging (Banfield et al. 1998). The occurrence of water clouds at p> 4 bar is also supported by the analysis of spectrally-resolved CH_3D line shapes at 2144 cm^{-1} (4.66 μm) (Bjoraker et al. 2015). Upper tropospheric and stratospheric hazes resulting from photochemical processes producing species like hydrazine and diphosphine are detected from their scattering in the most opaque regions of the spectrum, notably in the 4350 cm^{-1} (2.3 μm) methane band.

The spatial distribution of ammonia vapour has been investigated in both the upper troposphere (p < 1 bar, sounded in the thermal infrared, see Fletcher et al. (2016) and references therein) and at higher pressures in the lower troposphere (via Juno microwave sounding, Li et al. 2017). The most notable features are two ammonia-depleted bands at approximately 15S and 15N, corresponding to the South and North Equatorial Belts (SEB and NEB, respectively), which are seen as dark bands in the visible (see Rogers, 1995, for nomenclature of Jupiter's atmosphere features). These depletions appear to extend down to a several bars (Li et al. 2017; Grassi et al. 2020). Equatorial belts are locations of low aerosol content as well as of warmer air temperatures (e.g., Gierasch et al. 1986). Both facts suggest that the distribution of ammonia is driven by dynamics: indeed, if the ammonia distribution were driven by simple condensation, one would expect more ammonia in warmer, cloud-free regions. Fletcher et al. (2020) investigated in detail the correlation between air temperature, ammonia, and clouds in the region between the Equatorial Zone (EZ) and the NEB. The region is notable for the occurrence of a trapped Rossby wave that produces a variety of phenomena such as bright plumes (observed in the visible) and '5-μm hot spots' (seen in thermal infrared). The study demonstrated that, although a higher ammonia content is usually associated with

the most opaque and reflective regions, in a number of instances the correlation is rather weak.

Further constraints on the ammonia and cloud distributions can be provided by the daytime spectral measurements of the Jovian Infrared Auroral Mapper (JIRAM), on board the NASA Juno mission (Adriani et al. 2014). Specifically, the JIRAM spectral range spans between 1994 and 5017 cm^{-1} (5.01-1.99 μm); it includes therefore the 3125-4910 cm^{-1} (2.0-3.2 μm) region, dominated by reflected solar radiation (rather than by thermal radiation or auroras), which allows one to detect scattering occurring between 0.04 and 4 bars and to measure the ammonia absorption bands ν_1, ν_3, and $2\nu_4$, around 3300 cm^{-1} (3 μm). Moreover, radiance measured by JIRAM in the thermal range around 2000 cm^{-1} (5 μm) provides further constraints on aerosol opacities (Grassi et al. 2020). Unfortunately, the quantitative retrieval of cloud properties from scattering is a challenging task, due to uncertainties in a number of critical parameters that shape the final spectrum (scattering phase function, cross sections, single scattering albedo, all ultimately driven by composition, size and shape of aerosols, and their variations at different altitudes, e.g.: Sromovsky & Fry, 2010a) and to the inherent high-degeneracy of the inverse problem (different physical conditions may lead to similar spectra, indistinguishable within measurement uncertainties).

This work follows a preliminary effort by Sindoni et al. (2017), to exploit JIRAM daytime data on a larger scale. Our focus here is on low-latitude regions, where the comparison against previous studies from ground and space-borne instruments on clouds and ammonia is possible and very uniform observational conditions (emission, incidence and phase angles) were achieved during the first Juno perijove passage (PJ hereon) around Aug. 27th, 2016. Moreover, at low latitudes, residual contribution from auroral H_3^+ emissions at ~3125 cm^{-1} (3.2 μm) can safely be assumed as negligible. In section 2 we describe the JIRAM instrument and data, detailing the selection criteria for the observations considered in our analysis. In section 3 we discuss the model adopted to represent the Jupiter's atmosphere in our spectral simulations as well as the retrieval code developed to compute a set of physical parameters of the atmosphere from JIRAM data. Section 3 also presents the estimated errors on retrieved quantities. Section 4 shows the main results of our analysis, with maps of ammonia and of a few parameters representative of aerosol distribution in the upper troposphere. Beside large-scale maps between 25°N and 35°S, a few regions of potential interest are also presented. In section 5 we provide a short discussion on these results, with comparisons against other studies and interpretation in terms of global and regional dynamics.

2. JIRAM data

JIRAM (Adriani et al. 2014) consists of an infrared spectro-imager covering the 1994-5017 cm^{-1} (5.01-1.99 μm) range with a spectral sampling increasing from 7 to 22 cm^{-1}. The spectrometer simultaneously acquires 256 spectra, arranged along a line of spatially contiguous pixels (a 'slit'). JIRAM spectra are often complemented by context images obtained by integrating the incoming radiance over a broad spectral range centred around 2080 cm^{-1} (M-filter imager). The field of view of individual pixels (for the

spectrometer as well as for the imager) is about 240 μrad. Therefore, the field-of-view of the JIRAM spectrometer consists of an area of 1 x 256 pixels and covers an area on the celestial sphere of 240 μrad x 3.5° (being 3.5°= 256 x 240 μrad). Hereafter, unless otherwise specified, “JIRAM” stands for “JIRAM spectrometer”. Juno is a spinning spacecraft and the JIRAM pointing system has only one degree of freedom, the long direction of the slit being forced to be parallel to the Juno rotation axis. This implies that the slit can be placed arbitrarily over a band in the sky of width 3.5° having the Juno rotation axis as its polar axis (‘visibility strip’). Since JIRAM can acquire only one slit at each Juno spacecraft rotation (2 rpm), gaps or overlaps between slits from consecutive rotations may exist, depending upon the timing of the measurements. Consecutive slits are in general not spatially connected. Adriani et al. (2014) described the extensive on-ground spectral, geometric and radiometric calibrations performed on the JIRAM flight model prior to launch. In-flight calibration relies on periodic observations of internal calibration sources (high-temperature black bodies and deep space) to characterize and monitor long-term variations of instrument spectral responsivity, thermal background and read-out noise. The standard deviation of deep-sky observations during each observation session is employed for estimating the JIRAM Noise Equivalent Radiance (NER). We made a specific assessment that demonstrated that photon noise is a negligible component of NER for the data used in this study. It was also shown that NER increases dramatically for the last five spectral sampling points. We neglect therefore the data in the range 4930-5017 cm^{-1} (1.99-2.03 μm).

JIRAM observes Jupiter for short periods of about two days surrounding each PJ passage, which occurs every 53 days, Juno’s orbital period. JIRAM planning and commanding activities are extensively described in Noschese et al. (2020). Even during these PJ passages, Jupiter may often fall outside the ‘visibility strip’, because of specific spacecraft attitudes and the evolution of Juno’s orbit. The overall result is a relatively sparse spatial coverage, strongly variable from PJ to PJ, and variable viewing geometries. For this study, given the strong dependence of the signal in the solar spectral range upon incidence (i), emission (ε) and phase (φ) angles (Hanel et al. 2003, eq. 2.2.3), we found it appropriate to consider our analysis in a limited region of the space defined by these three angles. This allows one to minimize, at least for this effort, further complications related to the definition of aerosol scattering phase functions over large ranges of angles. A heuristic analysis of the distribution of data pointed toward a subset from PJ1, with $40° < i < 50°$, $40° < \varepsilon < 50°$, $\varphi \sim 90°$, as a fair choice. Both emission and incidence angles were kept as small as possible, to minimize modeling errors that are amplified by large optical paths. Spatial coverage is presented in Fig. 1, as resulting from 21163 JIRAM spectra. Data over the northern hemisphere were mostly acquired before the pericentre passage, between Aug. 25th, 2016, 22.45 UTC and Aug. 26th, 23.15 UTC, while data over the southern hemisphere were acquired shortly after the pericentre, between Aug. 27th, 20.55 UTC and Aug. 28th, 08.20 UTC. Spatial resolution is also variable: data acquired before pericentre (north) have a pixel size between 480 and 350 km (with few instances around 240 km), while those acquired after

the pericentre (south) offer a smaller pixel size, between 150 and 300 km. The degree of overlap (multiple observations of the same region) is marginal and found mostly in two regions south of 20°S; consequently, no effort was made to consider the different acquisition times and to compensate for mean zonal winds in order to refer longitudes to a given reference time.

However, these limited regions of overlap were essential for the detection of a signal bias correlated to the Juno position along the orbit. By comparing the mean spectra acquired over the same areas at different distances, we noticed an increase of the signal while closer to the perijove (See Fig. S1 in supplemental materials). This bias is relatively higher (but not limited) at higher wavenumbers (shorter wavelengths) and may induce systematic errors on the derived atmospheric quantities. In the Results section, we excluded the values derived from the spectra acquired at distances lower than $9x10^5$ km. The definition of such a threshold for these parameters is largely arbitrary: the amplitude of the bias, as estimated from the mean signal at 2900 cm^{-1} (3.44 μm, a spectral region of very low signal largely dominated by random signal fluctuations away from the poles) descends very slowly back to the pre-perijove, (and almost-constant) value during the post-perijove measurements. A total exclusion of these latter data would however spoil completely the coverage of the southern hemisphere. The ultimate cause for this bias remains to be clarified. The overall trend appears to be correlated with instrument temperatures, but no similar effects were observed in the 5-μm data considered in Grassi et al. 2020, in principle much more prone to thermal noise. Alternatively, the bias can be induced by the impinging of high energy particles while crossing through of the Jupiter magnetosphere.

System III (Archinal et al. 2011) West longitudes and planetocentric latitudes are used to denote geographic coordinates throughout this paper. JIRAM data used for this analysis are publicly available at the NASA Planetary Data System (Noschese & Adriani, 2017).

3. Spectral model and retrieval code

Two typical JIRAM spectra in the solar-dominated spectral range are presented in Fig. 2. For individual spectra, the signal between 4100 and 4610 cm^{-1} (2.44-2.17 μm) falls at the level of NER and therefore is not included in our analysis. Labels in the figure indicate the location of main gaseous absorptions. In our effort to model JIRAM data, we adopt a forward model based on the methods presented in Ignatiev et al. (2005). The forward model is a code used to compute the expected spectrum given a set (‘state vector’) of physical conditions of Jupiter’s atmosphere (and viewing conditions). Gaseous absorptions are treated according a correlated-k approach (Irwin et al. 2007) with 30 quadrature points. We take into account methane, hydrogen collision-induced absorption and ammonia, with the data sources listed in Grassi et al. (2017, 2010). Inclusion of a realistic content of phosphine in the upper troposphere, as given in Fletcher et al. (2016), is found not to provide significant improvement to the spectral fit (see Fig. S2 in supplemental materials). Phosphine was also neglected by Sromovsky & Fry (2010a) in their analysis of Jupiter VIMS data. Scattering is treated with the methods presented by Isaacs et al. (1987). In

Jupiter's upper troposphere, given the low absolute temperatures, aerosols are expected to be in solid form and not spherical liquid droplets. Consequently, our use of the Mie theory to derive extinction cross section (Q_{ext}), single scattering albedo (ω_0) and asymmetry parameter (g) for a Henyey-Greenstein phase function is only a crude approximation, justified only by the very limited available knowledge of actual non-spherical aerosol properties.

The definition of an appropriate state vector suitable to exploit the information content of the available data is a non-trivial task, given the number of different choices (e.g., the number of aerosol layers, the analytical shape that describes the aerosol density with altitude, etc.) that may lead to very similar results. Ambiguities in modelling Jupiter spectra in this spectral range are well illustrated by the variety of different models presented by Sromovsky & Fry (2010a) and Sromovsky & Fry (2010b). Eventually, we adopted the cloud scheme presented in Fig. 5.10 of West et. al. (2004). This scheme has the advantage that it summarizes a number of independent sources of information on Jupiter's clouds and has therefore a robust experimental basis. We consider (a) a middle cloud, putatively composed of solid NH_4SH, centred at about 1.3 bars; (b) an upper cloud, putatively composed of NH_3 ice, centred at about 0.6 bars; (c) a diffuse tropospheric haze, limited below the tropopause. The middle cloud base is expected to be located around 2.2 bars. Its base rises to 1.3 bar in conditions of relatively dry air, such as the ones found in hot spots (Irwin et al. 1998). Our choice is justified by the fact that, while our retrieval code is capable of adjusting the vertical location of the cloud centre, it is indeed most sensitive to the vertical location when clouds are thin. It is important to note that the altitude of the middle cloud is not constrained to remain at pressures less than 3 bars, and, as such, the middle cloud also represents deeper clouds in conditions of exceptional transparency. However, the sensitivity of data acquired in the spectral range of interest is expected to decrease significantly for pressures higher than 3 bar (see Fig. 3 in Irwin, 1999). We further elaborated the West et al. (2004) scheme by assuming - for both the middle and the upper clouds - Gaussian profiles for particle number density vs altitude. The tropospheric haze is assumed to have a number density constant along altitude (i.e.: a rectangular, slab-like profile). Stratospheric hazes contribute mostly in the region of low signal-to-noise ratio 4100-4650 cm^{-1} (2.44-2.15 μm) and are therefore not included in our model.

Other relevant features of our forward model pertain to the gaseous components. Methane is assumed to be uniformly mixed in the atmosphere, neglecting the stratospheric depletion due to photolysis, since it takes place at altitudes much higher than those probed by JIRAM measurements. H_2 ortho/para is assumed to be at its equilibrium value. Temperature vs. pressure profile is taken from Braude et al., 2020 and is assumed as latitude-independent , given the limited temperature variations (±4K) observed by Fletcher et al. (2016) at the 0.5-bar level. For the ammonia vertical distribution, following Fletcher et al. (2016), we consider a "deep" mixing ratio constant with altitude up to the 800-mb level. Above this level, the ammonia mixing ratio is assumed to decay according to a constant fractional scale height. Both the deep mixing ratio and the fractional scale height are free parameters adjusted to fit the data. We

adopted the Solar irradiance spectrum given by Makarova et al. (1974). No significant improvement in the fit quality was achieved considering the high-resolution solar spectrum presented by Fiorenza et al. (2005). Following Braude et al. (2020), the atmosphere is modelled as a stack of 39 levels spaced from 8.5 to $1.7x10^{-3}$ bars, with a denser grid where clouds are expected to occur.

The choice of the cloud structure is also supported by the results from a set (>100 cases) of our own forward simulations, performed to define reasonable first guesses for modelling on the basis of few test JIRAM spectra. The main lessons learned from these forward simulations can be summarized as follows:

a. The large range of pressures probed between 3650 and 3850 cm^{-1} (2.74-2.59 μm) (Fig. 1 in Sromovsky & Fry, 2010a) makes it problematic to model the observed JIRAM signal with a single, slab-like, cloud layer with variable altitude. The two-cloud (middle and upper) scheme of West et al. (2004) allows one to effectively adjust the ratio in the observed signal at the peak and in the wings of the 3650 cm^{-1} (2.74 μm) maximum. The occurrence of two distinct maxima in aerosol density is also consistent with recent results by Braude et al. (2020) from visible spectra.

b. We were not able to model JIRAM spectra adopting a middle cloud composed of ammonium hydrosulphide ice, at least by considering the refractive indices given in Howett et al. (2007). This compound invariably produces a shape of the reflectivity maximum at 3650 cm^{-1} (2.74 μm) that is much flatter than that observed in the data, regardless of the assumed effective radius or the presence of an ammonia ice coating (see Fig. S3 in supplemental material). Similarly, clouds composed of an ammonia ice core coated by water ice (or by a water ice core inside an ammonia ice coating) do not provide, in most circumstances, an adequate fit to the data. Scattering properties of the coated particles were estimated using the BART code (Quirantes-Sierra, 2007). Further tests on NH_3 ice particles coated by trace contaminants (e.g.: the material presented in Carlson et al. (2016) or soot/hydrocarbons precipitating from photochemically-active regions) are currently precluded by the absence in literature of refractive indices of these materials in the spectral range of our interest.

c. As pointed out by Sromovsky & Fry (2010b), the HITRAN database for ammonia appears to be incomplete for $\nu > 3450$ cm^{-1} ($\lambda < 2.9$ μm) and no significant updates for $\nu < 4000$ cm^{-1} ($\lambda > 2.5$ μm) are reported up to its latest release (Gordon et al. 2017). For this reason, in the $3450 < \nu < 4000$ cm^{-1} we considered entries from the EXOMOL database (Coles et al. 2018). Although this crude ammonia update indeed produces changes in JIRAM simulated spectra well above the NER level (and is therefore retained in subsequent analysis), it cannot offset by itself the flatness of a pure ammonium hydrosulphide cloud.

d. An upper cloud composed of pure ammonia ice produces, in several cases, a signal decrease from the maximum at 3650 cm^{-1} (2.74 μm) toward lower wavenumbers (higher wavelengths) steeper than observed in JIRAM spectra, regardless of whether the refractive indices of Howett et al. (2007) or Martonchik et al. (1984) are considered. For

sake of completeness, a full analysis of the dataset was performed assuming an upper cloud composed of pure ammonia ice with r_e = 3 μm. The quality of the fit, as quantified by χ^2/N values, albeit very similar in absolute terms, is found significantly better for the tholin model by a paired Student's t-test (the null hypothesis of equal means has a probability < 10^{-4})

Sromovsky & Fry (2010a) adopted ad hoc optical constants for the upper cloud in their model, in order to achieve the required absorption for ν < 3500 cm^{-1} (λ > 2.74 μm). In our work, to cope with previous points b. and d., we found it to be simpler to follow the approach proposed in Sindoni et al. (2017) and to consider tholin optical constants. Namely, we adopt the medium-pressure (MP) type described by Imanaka et al. (2012) for both the upper and the middle clouds (in Imanaka et al. (2012), 'medium pressure' describes the conditions of the irradiation chamber where tholin were produced and corresponds to 1.6 mbar). Although we do not propose Titan-like tholins as realistic analog for Jupiter's aerosol clouds, certain characteristics that they might share with aerosols in the hydrogen-rich atmosphere of Jupiter make them useful. Indeed, they are spectrally flat in most of the spectral region of our interest, with the exception of the large N-H stretching band starting at 3650 cm^{-1} (2.74 μm) and centreed at about 3400 cm^{-1} (2.94 μm) that, given the role that ammonia should realistically play in Jupiter aerosols, is likely to be responsible for the absorption seen in JIRAM spectra. For both the upper and middle clouds we adopted an effective radius r_e of 3 μm and a variance of 0.1. Direct tests demonstrated that the quality of fit, as quantified by χ^2/N values (and final retrieval results) is not significantly altered by the reduction of r_e of the upper cloud's particles down to 1 μm. The 1-3 μm range is consistent with the radius values retrieved by Braude et al. (2020) from spectroscopy in the visible range.

Other considerations that emerged from the forward simulations are:

e. The flatness and signal level observed between 3150 and 3330 cm^{-1} (3.17-3.0 μm) are the main rationale for the inclusion of the tropospheric haze. Following Sromovsky & Fry (2010b) (layer 2 in their Table 4), we considered a pure reflective aerosol with complex refractive index (n=1.4, k=0), r_e = 0.03 μm and a variance of 0.1.

f. The inclusion of tropospheric haze significantly increases the signal level around 4900 cm^{-1} (2.04 μm), but our simulations (as well as best fits presented later) remain systematically lower in radiance at this wavenumber compared to JIRAM data. This issue is solved either by the variations in r_e for clouds and haze explored in our forward tests nor by inclusion of stratospheric haze. Notably, no excess at 4900 cm^{-1} is reported by Sromovsky & Fry (2010a) and Sromovsky & Fry (2010b), suggesting therefore a role in assumed aerosol properties in causing the deficiency observed in our own simulations.

Moving to the actual retrieval scheme, we consider a total of 11 free parameters to be adjusted to match the observed JIRAM spectra: total optical thickness, central altitude and vertical dispersion (i.e. σ) for the Gaussian distributions of aerosol densities in upper and middle clouds (6 parameters); the total optical thickness, central altitude and vertical extension (i.e. half-width) for the

uniform (slab-like) distribution of tropospheric haze (3 parameters); and the deep mixing ratio and fractional scale height for ammonia (2 parameters). Figure 3 presents variations of the spectrum resulting from realistic variations of the parameters to be retrieved.

The free parameters are estimated via a Bayesian retrieval code conceptually identical to the one presented by Grassi et al. (2017) and derived from the general principles described in Rodgers (2000). Table S4 in supplemental materials provide details on the a priori (and initial) values adopted in the retrieval procedure and corresponding covariances. Formal retrieval errors related to random signal fluctuations (NER) can also be estimated on the basis of the Bayesian formalism, and as such are also listed in Table S4. These estimates however are poorly representative of the actual uncertainties. Firstly, as discussed in the section 4 below, the retrieval code is seldom capable of producing a difference between the observed and best-fitting data within NER levels. Secondly, the retrieval error on different parameters displays a non-negligible correlation (errors on different parameters can compensate reciprocally to produce a fair data fit, demonstrating therefore a degeneracy of the inverse problem). For examples, the statistical correlation indeed exceeds 0.8 among the different haze parameters, as well as among different upper clouds parameters. Thirdly, formal estimate of errors strongly depends upon the specific set of parameters defining the current conditions of the atmosphere (in the Bayesian nomenclature, upon the points in state space where Jacobians are computed), and is hardly representative of the entire population of cases.

Moreover, the physical interpretation of retrieved parameters requires particular care. Whenever the opacities of upper and middle clouds become optically thick ($\gtrsim$ 2), parameters describing deeper cloud densities become more and more uncertain. Namely, the middle cloud often reaches high opacity already in its uppermost levels above the putative maximum, and in these conditions its retrieved central altitude and total opacity are mere extrapolations inferred from the upper wing of the distribution, without any true significance. Another example is the lower boundary of tropospheric haze, that formally contributes to the haze slab vertical thickness, but is in fact not constrained by our data since it may easily occur at altitudes where the opacity of upper and middle clouds are dominant. Similarly, whenever the upper clouds become optically thick at pressures lower than 800 millibars, very little information can be inferred on the ammonia deep mixing ratio

To overcome these ambiguities, cloud, haze and ammonia parameters provided by the retrieval code are used to compute *derived* quantities. These derived quantities are conceived to be, as far as possible, dependent upon scattering/absorption occurring in the upper parts of the pressure range sensed by JIRAM data. Namely, these are 1) effective cloud altitude, defined as the altitude where τ@3650 cm^{-1} (2.74 μm) = 1 is achieved; 2) a very rough opacity scale height, defined as the difference between effective cloud top and the altitude where τ@3650 cm^{-1} (2.74 μm) = e (Euler's number) is achieved; 3) total opacity above the 1.3 bar level; 4) tropospheric haze opacity above the 200 mbar level; 5) ammonia relative humidity at the 500-millibar level. To compute ammonia relative humidity at a given level,

condensation of gaseous ammonia over its ice is assumed to follow the curve given in Glasser (2009). Ammonia relative humidity is estimated assuming the Braude et al. (2020) temperature profile, i.e.: ~134.4K at the 500-millibar level. The items (3) and (4) are referred to the 3650 cm^{-1} (2.74 μm) region, where atmospheric gases are more transparent. These derived quantities are the ones eventually presented in our Result section.

Uncertainties on derived quantities were estimated by direct numerical simulations, according the following steps: 1) we created a large random population (5000 cases) of sets of the eleven retrieval parameters previously described 2) each of these sets was used to compute the corresponding set of derived quantities 3) each of the sets at step 1 was used to compute the corresponding simulated spectrum; random noise with an amplitude corresponding to the NER was added to each spectrum 4) the spectra computed at step 3 were fed to the retrieval code 5) parameters retrieved at step 4 were used to compute corresponding derived quantities 6) derived quantities sets computed at steps 2 and 5 were compared one by one. This scheme provided following estimates of random uncertainties on derived parameters: 1) effective cloud altitude: ±2.5 km; 2) opacity scale height: ±3.6 km; 3) total opacity: ±1.6, increasing to ±3.6 for $\tau \sim 5$; 4) haze opacity: ±0.013; 5) ammonia relative humidity: ±16 per cent. The same test demonstrated that correlation among the errors on different derived quantities is always extremely low (0.04 at worse): degeneracy of inverse problem is therefore strongly mitigated by the usage of derived quantities rather than the direct use of the 11 parameters in the retrieval scheme.

The signal bias observed while in proximity of Jupiter and described in section 2 affects mostly the retrieved ammonia parameters, with anomalous increases (up to a factor 2) of relative humidity. Other derived quantities seems more robust against this instrumental effect. The ambiguity in ammonia remains the main rationale for the exclusion of near-perijove data from subsequent discussion.

Systematic errors may arise from a very large number of factors, notably the assumed aerosol properties. For example, the assumption of an upper cloud composed of pure ammonia ice instead of tholin induces a reduction of retrieved ammonia relative humidity by a factor ~0.7. As another example, an upper cloud composed of tholin particles with r_e = 1 μm induces an increase of retrieved value of total opacity by a factor 1.35 for $\tau < 5$. As already mentioned before, for both examples, final χ^2/N values are worse (according Student's T-test) than those provided by our reference model.

4. Results

Despite our best efforts in the preliminary definition of the state vector and on the assumptions concerning aerosols properties, our capability to fit the JIRAM data with our models remains modest. The black curve in Figure 4a presents the χ^2/N distribution for the population shown in Fig. 1, as computed in the ranges (3150-4100) and (4610-4930) cm^{-1} ((3.17-2.44) and (2.17-2.03) μm) with N = 87 (number of JIRAM sampling points considered in fit, 98, minus the number of free parameters to be retrieved, 11). Figure 4b and 4c offer two examples of spectral fit (high and low signal) with a χ^2/N value in the peak bin of histogram of Fig. 4a. Notably, the fit quality remains of the same order as that

achieved by Sromovsky & Fry (2010b). In a limited number of cases, fits were carried out with an independent retrieval code based on a Markov chain (from Tamminen & Kyrölä, 2001), returning very similar modeling performances. This test ruled out major limitations of the 'main' retrieval code in finding a best-fitting solution.

Figure 5 presents the mean and standard deviation of the residual (i.e. the difference between best-fitting and observed spectra) for the cases where $\chi^2/N < 200$. The mean can be seen as a systematic modeling error and its features are therefore common locations of excesses (e) or deficiencies (d) of radiance in best-fitting spectra when compared to JIRAM data. A number of notable small-scale details can be seen at 3620 (d), 3730 (d) and at 3800 (e) cm^{-1}. Larger-scale systematic discrepancies are found at 3250 (e), 3450 (d) and beyond 4800 cm^{-1} (d). The overall misfit is largely dominated by the spectral regions at the boundaries of the JIRAM range considered in our analysis. Once χ^2/N is considered in the 3350-4100 cm^{-1} (2.98-2.44 μm) region, we achieve a much more favorable statistic (blue curve in Fig.5a).

The systematic discrepancies in Fig. 5 translate into differences between observed and best-fitting spectra exceeding sometimes 20 per cent. Limitations in the simulation methods do not represent a likely explanation for systematic discrepancies. These are more likely related to spectral features in actual Jupiter aerosols which are not adequately represented in the adopted tholin (or 'flat' haze) model. Improvement in the assumption affecting these spectral region will represent a key test of future efforts, but our forward simulations so far have not been able to indicate where specific corrections should be made. The results of a few attempts are presented in Figure S5 in Supplemental Materials, although possible alternatives (as variations in composition, size, analytical form of vertical distributions) are so numerous that their systematic exploration is in fact extremely challenging.

Figure 6 presents the spatial distribution fit quality, as quantified both by χ^2/N and by the relative fit quality (as defined in eq. 1 of Grassi et al. 2020). The former compares the discrepancy to a fixed NER value, the latter to the current signal level. The comparison between the two panels is consistent with discrepancies driven by imperfect assumptions regarding scattering properties of clouds. These assumptions, when the observed radiance is dominated by reflection of solar photons, are expected to produce an amplitude of misfit that increases along with the signal (compare Fig. 6a and Fig. 1a). At the same time, the ratio of the discrepant fit to the signal remains almost constant, as indeed observed in our case.

We retain for further discussion only the spectral fits where $\chi^2/N < 200$ and fit parameter < 0.25. Maps of derived parameters are presented in Fig. 7-11, along with corresponding latitudinal averages. For each derived parameter, we present also the magnified maps of few regions of particular interest. It should be noted that for all latitudinal averages, the occurrence of the Great Red Spot (GRS) at about 20°S represents a potential complication in the interpretation of results. Consequently, data from longitudes between 300° and 330°W in the Southern hemisphere were not considered for the computation of these latitudinal profiles.

For sake of brevity, in the following discussion the terms “thermal signal” and “solar signal” are to be interpreted as the radiance measured by the JIRAM spectrometer at 2000 cm^{-1} (5 μm) and 3650 cm^{-1} (2.74 μm), respectively.

4.1 Ammonia

Figure 7 presents the ammonia relative humidity. The values range from 5 per cent to supersaturation for about 3 per cent of the cases. The NEB and SEB depletions inferred from mid-infrared measurements by Fletcher et al. 2016 (their Fig. 18b) are essentially confirmed in their position and values, especially upon taking into account the Cassini Composite Infrared Spectrometer data acquired during the 2000 Jupiter’s flyby. Also, the decrease to a latitudinally-constant value of about 60 per cent poleward of 25°S is a common feature of the two studies. The JIRAM-derived pattern appears somewhat compressed in latitude when compared to the one presented in Fletcher et al. 2016, with the former displaying peaks at 20° rather than 25°. Variable positions of the ammonia maximum at 25°N are possibly related to the periodic variations in size of the NEB (Fletcher et al. 2017). While the NEB was indeed contracting at the time of JIRAM observations, data presented here cover just a single Juno perijove passage and therefore can not provide a firm confirmation for this hypothesis. In the JIRAM map, the maximum over the equator is clearly lower (70 per cent) than as reported in Fletcher et al. 2016 (120 per cent). Our estimate of the amplitude of the equatorial peak is however hampered by the very limited number of spectra covering the area. Other notable features are the local ammonia maximum at 12°S and 16°S, within the general SEB depletion. These ammonia enhancements are associated with moderate-to-high thermal signal (in JIRAM M-filter context map) and dark color (in JunoCam context map), defining two distinct northern components of the SEB (compare Fig. 7a with Fig. 1a and Fig. 1b at 220°W and 180°W).

Contrary to the case of CIRS and TEXES data discussed in Fletcher et al., 2016, JIRAM data cannot provide a measurement of air temperatures and therefore a spectrum-by-spectrum, self-consistent, estimate of ammonia *relative humidity.* Once the latitude-independent air temperature value of Braude et al., 2020 is replaced by the CIRS-derived, latitude-dependent, air temperature values presented in Fletcher et al. 2016 (see Fig. S6 in supplemental materials), we observe a decrease of ammonia away from the EZ (where the temperature difference between the two profiles is minimal and well below 1K). In the CIRS-temperature assumption, while the overall pattern of “maxima over zones/minima over belts” remain preserved, we observe a deepening of minima over the equatorial belts as well as decreases of the maxima in both tropical zones. Namely, at 20°N, we have a reduction from 75% to 45%; on the south, the maximum moves from 75% at 20°S, to 50% at 25°S.

In the remaining discussion we consider the relative humidity values computed from the latitude-independent air temperature value of Braude et al., 2020. Indeed, this parameter remains proportional to the ammonia mixing ratio and allows one to compare different latitudes even in the absence of simultaneous estimates of air temperature.

The ammonia relative humidity also displays a notable longitudinal variability, better seen in the magnified regions.

Although JIRAM spectra offer only a partial coverage of the Oval BA and GRS (Fig. 7c), in both cases, the rims of these anticyclones appear depleted (25 per cent) in ammonia compared to surrounding latitudes. The very central part of Oval BA displays a value of about 70 per cent, consistent with the typical results we found at this latitude (30°S). The ammonia content in the inner parts of the GRS is apparently very low, but in fact this parameter is not constrained by our data since the reference altitude of 500 mb considered to estimate relative humidity is effectively masked by very high clouds found there. Ammonia depletions south and west of the GRS were previously reported by Fletcher et al. (2010) (fig. 4 there) and Fletcher et al. (2016) (Fig. 19a there).

The wake north-west of GRS (325°W, 15°S) displays a complex pattern for gaseous tropospheric ammonia: its average relative humidity is ~ 50 per cent, but the values computed from individual spectra vary between > 100 per cent and ~ 10 per cent. Similar strong variations are also seen around (355°W, 15°S). In both regions, higher values appear to be correlated to areas of low thermal/high solar signal, as inferred from JIRAM spectra. Context images acquired by JunoCam suggests that these ammonia-rich areas are associated with bright, whiter clouds in the SEB.

At 30°W and 70°W, we observe an increase in ammonia humidity up to ~ 100 per cent RH in a very narrow latitude band at about 18°S (Fig. 7d). A similar increase, albeit with smaller amplitude, is seen at other longitudes (e.g. 215°W) where JIRAM data cover this latitude. These enhancements contribute to create the maximum seen in latitudinal averages of Fig. 7b around 20°S. Context images by JunoCam during PJ1 offer here a rather coarse resolution, but best JIRAM M-filter images show a long string of turbulent features of similar size (red arrows in Fig. 7d). Higher ammonia content is apparently associated with the centres of these features, characterized by low thermal/high solar signal.

The northern border of the broad ammonia depletion centred at 15°N appears rather sharp, and follows the slight variations over different longitudes at the latitude corresponding to NEB's boundary, as the latter can be inferred from the solar signal (compare Fig. 7a and Fig. 1b). Unfortunately, the JIRAM data considered here do not cover any of the brightest hot spots occurring on Jupiter during PJ1 (see Fig. 1 in Grassi et al. 2020). However, the JIRAM data include the region at (155°W, 7.5°N) (red arrow in Fig. 7e), located immediately west of a hot spot of moderate brightness centred at about (165°W, 7.5°N). The region at (155°W, 7.5°N) displays a very high ammonia content (relative humidity > 100 per cent) and again low thermal/high solar signal.

4.2 Cloud effective altitude

Figure 8 presents the cloud effective altitude, in reference to the 1-bar surface. This parameter, as defined in section 3 on the basis of total integrated opacity, does not discriminate between the 'upper' and 'middle' clouds of our model. The altitude ranges usually from -5 km (p ~1.2 bars) in the South Temperate Belt (STB) to > 20 km (p < 0.4 bar) over the GRS. The height is > 15 km (p < 0.5 bar) over the northern part of EZ, with a clear hemispherical asymmetry

north and south of the equator in the EZ. North and South Tropical Zones (NTrZ and STrZ) are both locations of maxima in latitude profile. In the southern hemisphere, cloud height seems to decrease gradually from 20°S to 30°S, and then more abruptly toward higher latitudes. We also observe a local maximum in cloud altitudes at about 11°S in Fig. 8b. This feature represents a notable exception to the anticorrelation observed between cloud altitude and thermal signal at larger latitudinal scale, being indeed associated with a thermal signal maximum (compare Fig. 8a and Fig. 1b at 220°W). Similarly, the adjacent cloud altitude minimum at 14°S is located in an area of low thermal (and high solar) signal.

In Fig. 8c we observe the Oval BA structure: in its central core, clouds lie at about 12 km in altitude (p ~0.6 bar), surrounded by an annulus where their altitude reaches 17 km (p ~0.48 bar). An annular structure over Oval BA as a darker, redder ring is seen both in context JunoCam mosaic (albeit affected by moderate spatial resolution) as well as in early 2016 observations from the ground (see fig. 12 in Rogers and Adamoli, 2016). A thin annulus with slightly depressed clouds is consistently observed all around the Oval BA (it crosses both 345°W, 26°S and 340°W, 30°S). The GRS displays a sharp rise in cloud altitude, in agreement with a number of previous studies (e.g. Banfield et al. 1998), that found this structure standing higher than the surrounding regions. The GRS wake displays cloud altitudes typically ~10 km (p ~0.65 bar); however, around (323°W, 15°S) (blue arrow in Fig. 8c) we note extremely low values, down to -10 km, (p ~1.2 bar) and even three instances where inferred total opacity remains <1 and therefore cloud altitude can not be defined. The area displays high thermal and low solar signal; an example spectrum from there is shown in Fig. 4c.

The boundary between the EZ and the NEB hosts a number of spatially limited regions that display sudden rises in cloud altitudes (e.g.: (155°W, 7.5°N) and (203°W, 7.5°N) marked by red arrows in Fig. 8d and again at (250°W, 7°N)). These regions are associated with local increases in solar signal, very low thermal signal and often to local increases in ammonia relative humidity (compare Fig. 8d and Fig. 7e).

4.3 Opacity scale height

Figure 9 presents the opacity scale height. This parameter, as defined in section 3, refers to aerosol vertical distribution and shall not be confused with gaseous atmospheric scale height. Clouds are more vertically compact (low scale height) over the zones and more vertically extended (high scale height) over the belts. The values derived for this parameter are - in most circumstances – anti-correlated with solar signal (compare Fig. 9a and Fig. 1a), i.e.: compact clouds tend usually to be brighter. This anticorrelation is particularly evident in the small details seen on the SEB away from the GRS. The scale height displays a clear contrast between the two hemispheres: in the NEB, this parameter never exceeds 12 km, while on the SEB it reaches values of 20 km. The local minimum at 14°S corresponds to the minimum in cloud altitude at the same latitude previously described in Fig. 8a.

While clouds appear consistently more compact (scale height < 5 km) over the entire STrZ, the longitudinal variations of scale height are noticeable between 20°S and 20°N. The GRS is surrounded by clouds with

intermediate scale height of ~15 km. The external ring of the GRS itself (Fig. 9c) appears more compact (scale height < 5 km), while clouds in the central parts seem more extended in altitude (scale height of ~15 km). The region (323°W, 15°S) (blue arrow in Fig. 9c), previously noted for very low cloud altitudes, displays compact clouds with scale heights <5 km. Oval BA shows weak increase of aerosol scale height in the high cloud altitude annulus.

In the NEB, areas with higher scale height follow the variations of the boundary between the NEB and the NTrZ along longitude (compare 105°W and 255°W in Fig. 9a and 1b, with the latter region displaying a boundary clearly displaced toward the equator). From Fig. 9d, we note that limited areas with high-altitude clouds at 7.5°N previously described from Fig. 8d (red arrows on both figures) consistently display relatively extended clouds (scale height ~15 km). The correlation between scale height and altitude is however very weak over larger regions (e.g.: (200°W, 15°N) and (50°W, 15°N)).

4.4 Total aerosol optical thickness

Figure 10 presents the total aerosol optical thickness (τ_{clouds}) at 3650 cm^{-1} (2.74 µm) for altitudes above the 1.3-bar level. Most JIRAM spectra cover regions where $\tau_{clouds} \gtrsim 5$ is achieved well above the adopted reference level. In these cases, as already mentioned in section 3, the computed τ_{clouds} is indeed an extrapolation that relies heavily on assumed vertical profiles of cloud densities. The map is therefore conceived to highlight the regions with overall thinner cloud coverage, where τ_{clouds} is better constrained by data, and to allow one to correlate them with thermal signal level presented in Fig. 1b. At global level, confirming previous studies (among the most recent, Braude et al. 2020), the highest opacities occur over the zones. JIRAM data suggest lower opacities over the SEB than over the NEB. Most of the clearest regions (τ_{clouds} ~1.5) are indeed found at 17°S (e.g.: 35°W, see Fig. 10c), where the highest thermal emission at 5 µm (a piece of information not used in our retrievals) is measured.

The anticorrelation between thermal brightness and τ_{clouds} also holds at smaller scales. The wake of GRS hosts several relatively low τ_{clouds} regions, where the one at (15°S, 323°W) (blue arrow in Fig. 10d) stands out as among the most transparent ones (τ_{clouds} <1). The areas at (155°W, 7.5°N) and (203°W, 7.5°N) (arrows in Fig. 10e), previously noted for their high (Fig. 8d) and extended (Fig. 9d) clouds, display values of $\tau_{clouds} > 5$.

4.5 Total haze optical thickness

Figure 11 presents the total haze optical thickness (τ_{haze}) at 3650 cm^{-1} for altitudes above the 0.2-bar level. This pressure level is selected to be located, in most circumstances, above the effective altitude of higher clouds. However, it should be noted that at locations where cloud effective altitude reaches very high values (notably the inner parts of GRS, see Fig. 8c) our code fails to compute τ_{haze}. Highest τ_{haze} values (~ 0.1) are found above the EZ, in agreement with Braude et al. (2020) (see their figure 20). Notably, haze enhancement is confined to the northern part of the EZ, confirming the results summarized in the scheme of West et al. (2004). Numerical simulations described in section 3 suggest that - in principle – the retrieval code is able to disentangle an increase of haze optical thickness from an altitude increase of

the upper cloud. However, given the uncertainties on actual optical properties, size and vertical distribution of the two aerosol populations, we can not rule out that the haze enhancement over EZ is, at least partially, related to the upper-altitude trail off of particles in the upper cloud. Haze enhancements are also seen over both NTrZ and STrZ, as previously reported from thermal-IR data.

The value of τ_{haze} is high (0.1) in the entire visible rim of the GRS (Fig. 11c), with no relevant details being observed in the wake region. The core of Oval BA displays high τ_{haze} (0.1) and is surrounded by an annulus (of higher cloud altitude, as seen in Fig. 8c) apparently clear of haze. As mentioned above, this depletion is probably just a result of the limitation of our retrieval code to constrain τ_{haze} in conditions of very high clouds. The annulus itself is eventually surrounded by a second, more external annulus of moderate τ_{haze} (0.05). Over the EZ τ_{haze} displays a series of discrete local maxima (e.g.: (345°W, 5°N), see arrow in Fig. 11d and (50°W, 5°N)), with no obvious relation to ammonia or cloud features.

5. Discussion

The scheme of a Hadley-type circulation in the troposphere of Jupiter, with uplift occurring in zones and subsidence in belts has been proposed for a long time (Hess & Panofsky, 1951). Several authors presented a number of atmospheric parameter maps (notably, air temperatures at different altitudes) supporting this scenario (Gierasch, 1986; Simon-Miller et al. 2006; Achterberg et al. 2006; Fletcher et al. 2009, 2016). This scheme is in agreement with our results on cloud altitudes, which consistently appear higher over the zones. The larger values of opacity effective scale height (more extended clouds) observed over the SEB (~ 17 km) with respect to the NEB (~ 10 km), as well as the higher cloud altitude and haze opacity (15 km, 0.08) in the northern part of the EZ with respect to its southern part (10 km, 0.02), are consistent with a more vigorous vertical circulation in the northern hemisphere. Enhanced upwelling over a zone (in comparison to other zones or other parts of the same zone) may indeed contribute to lift higher the (upper) clouds there, as well as to prevent sedimentation of haze below the reference level. Enhanced downwelling over a belt (in comparison to other belts) may contribute to pushing the hazes down below the reference level, to diminishing and narrowing the residual clouds, as well as to inhibit the rising of disequilibrium species from deeper levels. This is indeed consistent with a deep local minimum of phosphine detected at ~10°N at 3-4 bars (Grassi et al, 2020) derived from the same data considered in this study. Alternatively, hemispherical asymmetry in cloud structure may result from the hemispherical asymmetry in air temperatures in upper troposphere (and hence of in condensation efficiency) inferred from thermal infrared data (Simon-Miller et al, 2006, Fletcher et al. 2016). JIRAM data analysed so far do not allow us to discriminate between cloud structure hemispherical asymmetry being a permanent feature or related to long-term cycles of activity of the equatorial belts (Fletcher, 2017; Antuñano et al. 2019). The warmer air temperatures found by Fletcher et al. (2016) in the upper troposphere over the NEB compared to the SEB suggest however that this asymmetry has existed at least since the year 2000.

As already mentioned in the introduction, the large-scale latitudinal trends of ammonia found by Fletcher et al. (2016), and confirmed by our results, points toward a global distribution of this molecule driven by dynamical factors rather than condensation processes. Extraction of ammonia from a deep reservoir in uplifting zones (Gierasch et al. 1986) is consistent with patterns presented in Fig. 7. In the assumption that - despite the lack of clear spectroscopic signatures - ammonia represents a major component of clouds, correlation between the ammonia relative humidity and tropospheric cloud opacity at p<1.2 bar (compare Fig.7a and 10a) further supports the view of an ammonia distribution driven more by vertical dynamics than a simple temperature-dependent condensation level. The results on ammonia abundances at deeper altitudes/higher pressures (3-10 bars) presented by Li et al. (2017) from Juno Microwave Radiometer data display however only very modest – if any - increases of ammonia at the locations of tropical zones. While this may appear to contradict the role of uplift, it is important to recognize that several mechanisms capable of modifying the ammonia mixing ratio to great depths in the troposphere have been proposed (Showman and de Pater, 2005, Guillot et al. 2020). The ammonia relative humidity (Fig. 7) is well correlated with tropospheric haze opacity (Fig. 11). This is consistent with tropospheric haze being composed of ammonia itself or the ultimate result of photodissociation processes of ammonia. It should be noted however that JIRAM spectra do not display the hydrazine ice features expected at 3190 and 3305 cm^{-1}.

Long-term record of visible observations demonstrate the variability of the SEB: sometimes a series of distinct narrow longitudinal ‘lanes’ can be observed, other times these are disturbed by small-scale outbursts of plumes and eddies. At the time of JIRAM observations, the latitude strip around 14°S displays low-altitude (between 0 and -7km), compact and thick clouds (as demonstrated by low thermal signal), that appears relatively bright for SEB conditions both in JunoCam images as well as in JIRAM spectra at 3650 cm^{-1}. This strip is bounded by two regions of higher (10 km), but more diffuse and thinner clouds at 11°S and 16°S. Both these latitudes display local increase of ammonia and appear relatively dark in JunoCam and ground based images (Rogers and Adamoli, 2016, fig. 12 there) and bright at 5000 cm^{-1}, as observed in JIRAM images and spectra. Overall, our observations are therefore consistent with a ‘distinct lanes’ phase of SEB activity. Although available air temperature latitudinal profiles (Porco et al, 2003; Fletcher et al. 2016) do not have a spatial resolution sufficient to clarify the nature of vertical motions within this belt, the local inflections seen at these latitudes in wind latitudinal profile presented by (Porco et al, 2003) point indeed to the occurrence of a weaker secondary circulation.

Figure 12 shows the longitudinal profiles of ammonia relative humidity and cloud altitude along a longitudinal cross-section of oval BA, with the corresponding signal measured at 3650 cm^{-1}. These trends would be consistent with a rise of cold air occurring at about 343°W, with an ammonia depletion due to condensation in the rising column. However, no simultaneous measurements of the air temperature at adequate spatial resolution are available in the outer rims of the oval BA to support this interpretation. In the JunoCam images, this distance from the

centre of oval BA corresponds to the outer, redder ring of the feature, about 3° from feature centre. This would be consistent with a circulation scheme similar to the one described for the GRS in de Pater et al (2010, fig 16c there) rather than the one proposed for Oval BA in the same work, the latter being also supported by the analysis of Wong et al. (2011). Radial profiles for ammonia and hazes can not be determined over the GRS due to the limitations in our algorithm previously described. The trend of effective cloud altitude (not shown) does not suggest any external ring of higher altitude: to the contrary, after an abrupt rise (from 12 to 29 km in less than 0.5° in longitude), clouds slowly continue to increase their altitude of about 2 km toward the GRS centre. This trend is consistent with the expectations of the model by Palotai et al. (2014), where density of the cloud increases monotonically toward the centre along the longitudinal GRS section. Notably, ground images show a clear reddening of the central part of the GRS at least until June 2016 (see fig. 21 in Rogers and Adamoli, 2016).

The region near (323°W, 15°S) is notable for its very low solar signal, very high thermal signal implying a very low opacity, such that in few instances the condition $\tau=1$ defining cloud altitude is not achieved at all. Overall, the scenario is consistent with an exceptional absence of clouds. The region is extremely uniform in the haze map, suggesting that mechanisms that create the cloud void are essentially operating below the 200 millibar level. The horizontal location of this region is consistent (as albedo patterns with respect to the GRS) with the site of the deep (~4 bar) cloud described by Banfield et al. (1998). A smaller region with similar properties (spectral radiances, derived parameters) is seen at 32°W, 18°S.

The local ammonia increase described in Fig. 7e is reminiscent of the ammonia enhancements presented in Fig. 14 of Fletcher et al. (2020). The identification of the JIRAM feature as a ‘plume’ associated to hot-spots is further supported by the increase of solar signal observed by JIRAM at the same location. While this individual instance can hardly be representative of the complex hot spot phenomenology, we note that the concomitant increase in cloud altitude is indeed consistent with the air parcel uplift expected by Friedson (2005) in the regions between individual hot spots.

6. Conclusions

The fits to the JIRAM data are not yet fully satisfactory, suggesting that some of our underlying assumptions will need be revised. These include: a) the use, as ‘instrumental’ analogue material for clouds, of photochemically produced aerosols (tholin) in the nitrogen-rich and ammonia-poor atmosphere of Titan, b) a simple model for the vertical distribution of ammonia, c) simplified phase function and scattering algorithms, to achieve acceptable processing time.

The complex interaction of ammonia and water in producing multiple phases of liquid and solid over an extended region, including “mushballs” that can sequester significant amount of ammonia vapor (Guillot et al. 2020) need to be considered, to compute more realistic scattering and absorption properties of aerosols to be tested against the JIRAM data. The apparent lack of ammonium hydrosulphide clouds in sufficient abundance to affect the spectrum is

significant, and requires modelling to focus on the interaction of ammonia, sulphur and water in forming clouds in the Jovian troposphere. On the other hand, we should mention again the factors that may have prevented us a satisfactory data modeling using ammonium hydro-sulfide, even in presence of possible significant amounts of this ice. These include masking by contaminant coatings (an extension of the data by Carlson et al. (2016) toward the infrared to at least 3.5 μm would be particularly important), non-spherical particles, amorphous rather than polycrystalline state for the ice (with significant implications on optical constants, as discussed in Howett et al. 2007).

Despite these limitations, the JIRAM dataset demonstrated its capability to constrain clouds and ammonia properties in the upper troposphere over a large range of latitudes. Our findings are in general consistent with the dynamical scenarios proposed in literature both at global (belt/zone patterns) as well as at local scale (GRS, plumes). Quantities derived from JIRAM retrievals points toward peculiar dynamical phenomena in the centre of the SEBand within at the Oval BA, and could represent useful constraints for future theoretical efforts that however far exceed the scope of this paper.

Future lines of work include the simultaneous fit of JIRAM data over its full spectral range and from different perijove passages, making use of both the solar and thermal signal and in different viewing conditions, to aid in clarifying some of the modelling ambiguities encountered in this effort.

Data availability

The data underlying this article are available in NASA Planetary Data System at https://pds-atmospheres.nmsu.edu/data_and_services/atmospheres_data/JUNO/jiram.html, and can be accessed with identifier JNO-J-JIRAM-3-RDR-V1.0

Acknowledgements

This work was supported by the Italian Space Agency through ASI-INAF contract 2016-23-H.1-2018.

S. K. Atreya and J. I. Lunine were supported through the Juno Project.

L. N. Fletcher is supported by a Royal Society Research Fellowship and European Research Council Consolidator Grant (under the European Union's Horizon 2020 research and innovation programme, grant agreement No 723890) at the University of Leicester.

G. S. Orton is supported by funds from NASA distributed to the Jet Propulsion Laboratory, California Institute of Technology.

We thank N. Ignatiev (IKI, Moscow) for the permission to use his radiative transfer subroutines and his kind help in code development.

We thank J. Rogers (British Astronomical Association) for his contribution in producing the JunoCam global map and his advice on ground observations.

We thank L. Kedziora-Chudczer (UNSW, Australia), E. D'Aversa and F. Oliva (IAPS-INAF) for useful discussion on data modeling.

JIRAM has been developed by Leonardo S.p.A. at the Officine Galileo - Campi Bisenzio site.

We are grateful to Angioletta Coradini (2046-2011), our late collaborator and director, for her foresight and determination that made possible the realization of JIRAM and its operation on board the Juno mission.

References

Achterberg R.~K., Conrath B. J., Gierasch P. J., 2006, Icar, 182, 169. doi:10.1016/j.icarus.2005.12.020

Adriani A., Filacchione G., Di Iorio T., Turrini D., Noschese R., Cicchetti A., Grassi D., et al., 2017, SSRv, 213, 393. doi:10.1007/s11214-014-0094-y

Adriani A., Moriconi M. L., Mura A., Tosi F., Sindoni G., Noschese R., Cicchetti A., et al., 2016, Ap&SS, 361, 272. doi:10.1007/s10509-016-2842-9

Antuñano A., Fletcher L. N., Orton G. S., Melin H., Milan S., Rogers J., Greathouse T., et al., 2019, AJ, 158, 130. doi:10.3847/1538-3881/ab2cd6

Archinal B. A., A'Hearn M. F., Bowell E., Conrad A., Consolmagno G. J., Courtin R., Fukushima T., et al., 2011, CeMDA, 109, 101. doi:10.1007/s10569-010-9320-4

Atreya S. K., Wong M. H., Owen T. C., Mahaffy P. R., Niemann H. B., de Pater I., Drossart P., et al., 1999, P&SS, 47, 1243. doi:10.1016/S0032-0633(99)00047-1

Baines K. H., Carlson R. W., Kamp L. W., 2002, Icar, 159, 74. doi:10.1006/icar.2002.6901

Banfield D., Gierasch P. J., Bell M., Ustinov E., Ingersoll A. P., Vasavada A. R., West R. A., et al., 1998, Icar, 135, 230. doi:10.1006/icar.1998.5985

Bjoraker G. L., Wong M. H., de Pater I., Ádámkovics M., 2015, ApJ, 810, 122. doi:10.1088/0004-637X/810/2/122

Braude A. S., Irwin P. G. J., Orton G. S., Fletcher L. N., 2020, Icar, 338, 113589. doi:10.1016/j.icarus.2019.113589

Carlson R. W., Baines K. H., Anderson M. S., Filacchione G., Simon A. A., 2016, Icar, 274, 106. doi:10.1016/j.icarus.2016.03.008

Coles P. A., Ovsyannikov R. I., Polyansky O. L., Yurchenko S. N., Tennyson J., 2018, JQSRT, 219, 199. doi:10.1016/j.jqsrt.2018.07.022

de Pater I., Wong M. H., Marcus P., Luszcz-Cook S., Ádámkovics M., Conrad A., Asay-Davis X., et al., 2010, Icar, 210, 742. doi:10.1016/j.icarus.2010.07.027

Fletcher L. N., Orton G. S., Mousis O., Yanamandra-Fisher P., Parrish P. D., Irwin P. G. J., Fisher B. M., et al., 2010, Icar, 208, 306. doi:10.1016/j.icarus.2010.01.005

Fletcher L. N., Greathouse T. K., Orton G. S., Sinclair J. A., Giles R. S., Irwin P. G. J., Encrenaz T., 2016, Icar, 278, 128. doi:10.1016/j.icarus.2016.06.008

Fletcher L. N., 2017, GeoRL, 44, 4725. doi:10.1002/2017GL073806

Fletcher L. N., Orton G. S., Greathouse T. K., Rogers J. H., Zhang Z., Oyafuso F. A., Eichstädt, G., et al., 2020, JGRE, 125, e06399. doi:10.1029/2020JE006399

Friedson A. J., 2005, Icar, 177, 1. doi:10.1016/j.icarus.2005.03.004

Gierasch P. J., Conrath B. J., Magalhães J. A., 1986, Icar, 67, 456. doi:10.1016/0019-1035(86)90125-9

Glasser L., 2009, JChEd, 86, 1457. doi:10.1021/ed086p1457

Gordon I. E., Rothman L. S., Hill C., Kochanov R. V., Tan Y., Bernath P. F., Birk M., et al., 2017, JQSRT, 203, 3. doi:10.1016/j.jqsrt.2017.06.038

Grassi D., Adriani A., Mura A., Atreya S. K., Fletcher L. N., Lunine J. I., Orton G. S., et al., 2020, JGRE, 125, e06206. doi:10.1029/2019JE006206

Guillot T., Li C., Bolton S. J., Brown S. T., Ingersoll A. P., Janssen M. A., Levin S. M., et al., 2020, JGRE, 125, e06404. doi:10.1029/2020JE006404

Hanel R. A., Conrath B. J., Jennings D. E., Samuelson R. E., 2003, Exploration of the Solar System by Infrared Remote Sensing, Cambridge University Press, Cambridge

Hess, S. L., and Panofsky, H. A., 1951, in Malone T.F. ed., Compendium of Meteorology, American Meteorological Society, Boston

Howett C. J. A., Carlson R. W., Irwin P. G. J., Calcutt S. B., 2007, JOSAB, 24, 126. doi:10.1364/JOSAB.24.000126

Imanaka H., Cruikshank D. P., Khare B. N., McKay C. P., 2012, Icar, 218, 247. doi:10.1016/j.icarus.2011.11.018

Ignatiev N. I., Grassi D., Zasova L. V., 2005, P&SS, 53, 1035. doi:10.1016/j.pss.2004.12.009

Irwin P. G. J., Weir A. L., Smith S. E., Taylor F. W., Lambert A. L., Calcutt S. B., Cameron-Smith P. J., et al., 1998, JGR, 103, 23001. doi:10.1029/98JE00948

Irwin, P.G.J., 1999, Surveys in Geophysics 20, 505–535, doi:10.1023/A:1006662811248

Irwin P. G. J., Teanby N. A., de Kok R., Fletcher L. N., Howett C. J. A., Tsang C. C. C., Wilson C. F., et al., 2008, JQSRT, 109, 1136. doi:10.1016/j.jqsrt.2007.11.006

Isaacs R. G., Wang W.-C., Worsham R. D., Goldenberg S., 1987, ApOpt, 26, 1272. doi:10.1364/AO.26.001272

Li C., Ingersoll A., Janssen M., Levin S., Bolton S., Adumitroaie V., Allison M., et al., 2017, GeoRL, 44, 5317. doi:10.1002/2017GL073159

Noschese, R., and Adriani, A., 2017, https://pds-atmospheres.nmsu.edu/data_and_services/atmospheres_data/JUNO/jiram.html

Noschese R., Cicchetti A., Sordini R., Cartacci M., Mura A., Brooks S., Lastri M., et al., 2020, AdSpR, 65, 598. doi:10.1016/j.asr.2019.09.052

Martonchik J. V., Orton G. S., Appleby J. F., 1984, ApOpt, 23, 541. doi:10.1364/AO.23.000541

Palotai C., Dowling T. E., Fletcher L. N., 2014, Icar, 232, 141. doi:10.1016/j.icarus.2014.01.005

Porco C. C., West R. A., McEwen A., Del Genio A. D., Ingersoll A. P., Thomas P., Squyres S., et al., 2003, Sci, 299, 1541. doi:10.1126/science.1079462

Quirantes-Sierra, A. (2007) http://www.ugr.es/~aquiran/ciencia/codigos/bart.f

Rodgers, C. R., 2000, Inverse methods for atmospheric sounding: Theory and practice, World Scientific, Singapore

Rogers, J. H., 1995, The Giant Planet Jupiter, Cambridge University Press, Cambridge

Rogers, J. H and Adamoli, G., 2016, https://britastro.org/node/8263

Seiff A., Kirk D. B., Knight T. C. D., Young R. E., Mihalov J. D., Young L. A., Milos F. S., et al., 1998, JGR, 103, 22857. doi:10.1029/98JE01766

Showman A. P., de Pater I., 2005, Icar, 174, 192. doi:10.1016/j.icarus.2004.10.004

Simon-Miller A. A., Conrath B. J., Gierasch P. J., Orton G. S., Achterberg R. K., Flasar F. M., Fisher B. M., 2006, Icar, 180, 98. doi:10.1016/j.icarus.2005.07.019

Sindoni G., Grassi D., Adriani A., Mura A., Moriconi M. L., Dinelli B. M., Filacchione G., et al., 2017, GeoRL, 44, 4660. doi:10.1002/2017GL072940

Sromovsky L. A., Fry P. M., 2010a, Icar, 210, 230. doi:10.1016/j.icarus.2010.06.039

Sromovsky L. A., Fry P. M., 2010b, Icar, 210, 211. doi:10.1016/j.icarus.2010.06.040

Taylor F. W., Atreya S. K., Encrenaz T., Hunten D. M., Irwin P. G. J., Owen T. C., 2007, in Bagenal F., Dowling T. and McKinnon W. ed., Jupiter, the Planet, Satellite and Magnetosphere, Cambridge University Press, Cambridge, p59

Tamminen, J., and Kyrölä, E. 2001, JGR, 106, 14,377. doi:10.1029/2001JD900007

West R. A., Baines K. H., Friedson A. J., Banfield D., Ragent B., Taylor F. W., 2007, in Bagenal F., Dowling T. and McKinnon W. ed., Jupiter, the Planet, Satellite and Magnetosphere, Cambridge University Press, Cambridge, p79

Wong M. H., de Pater I., Asay-Davis X., Marcus P. S., Go C. Y., 2011, Icar, 215, 211. doi:10.1016/j.icarus.2011.06.032

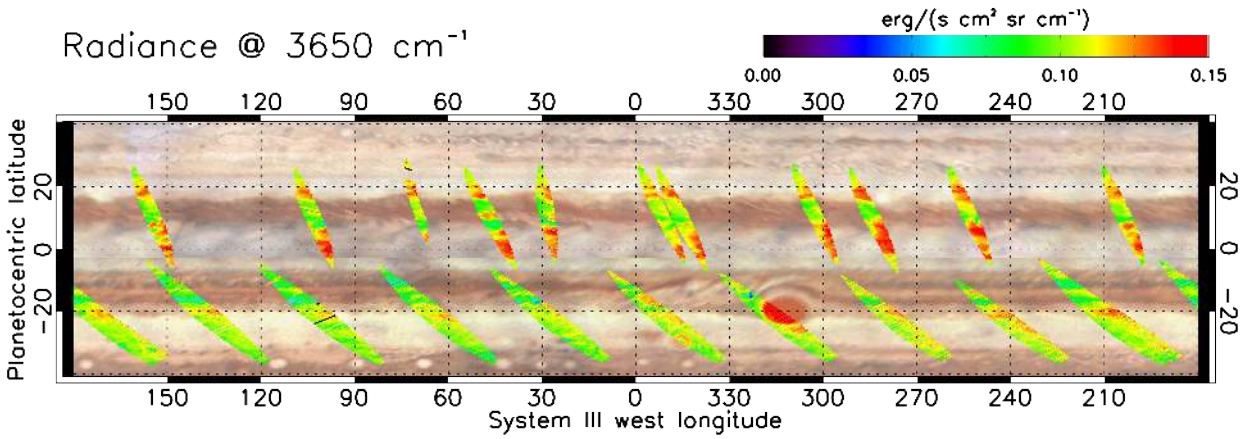

a

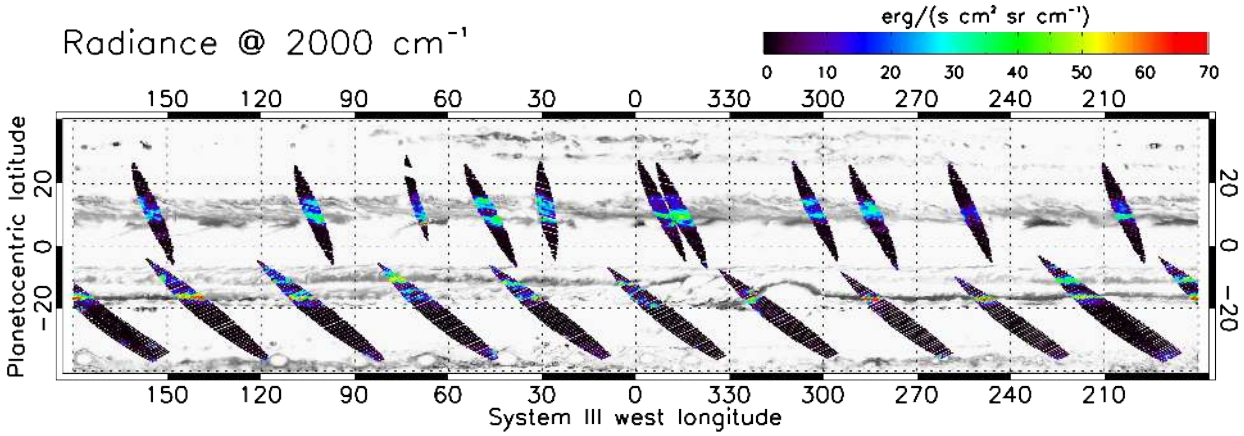

b

Fig. 1. Spatial distribution of JIRAM *spectra* considered in this work.
Panel a. Signal measured by JIRAM spectrometer at 3650 cm^{-1} and, as background, a global map created from visible images acquired by the JunoCam.
Panel b. Signal measured by JIRAM spectrometer at 2000 cm^{-1} and, as background, a global map created from infrared *images* acquired by the JIRAM M-channel imager. To improve readability, gray scale of the latter has been inverted (black = more signal, white = less signal). The color code presented in the upper-right bar refers strictly to the signal measured by the JIRAM spectrometer and does not apply to the JIRAM imager background.
JIRAM data were acquired during the first Juno perijove passage (PJ1), around Aug. 27th, 2016, over a time span of about 2.5 Earth days. Notably, both background images are mosaics of individual images acquired over similar time spans, and slight longitude mismatch of features may occur between different datasets because of large-scale motions related to zonal winds.
In these maps, the actual area covered by each individual spectra is slightly exaggerated to improve readability.

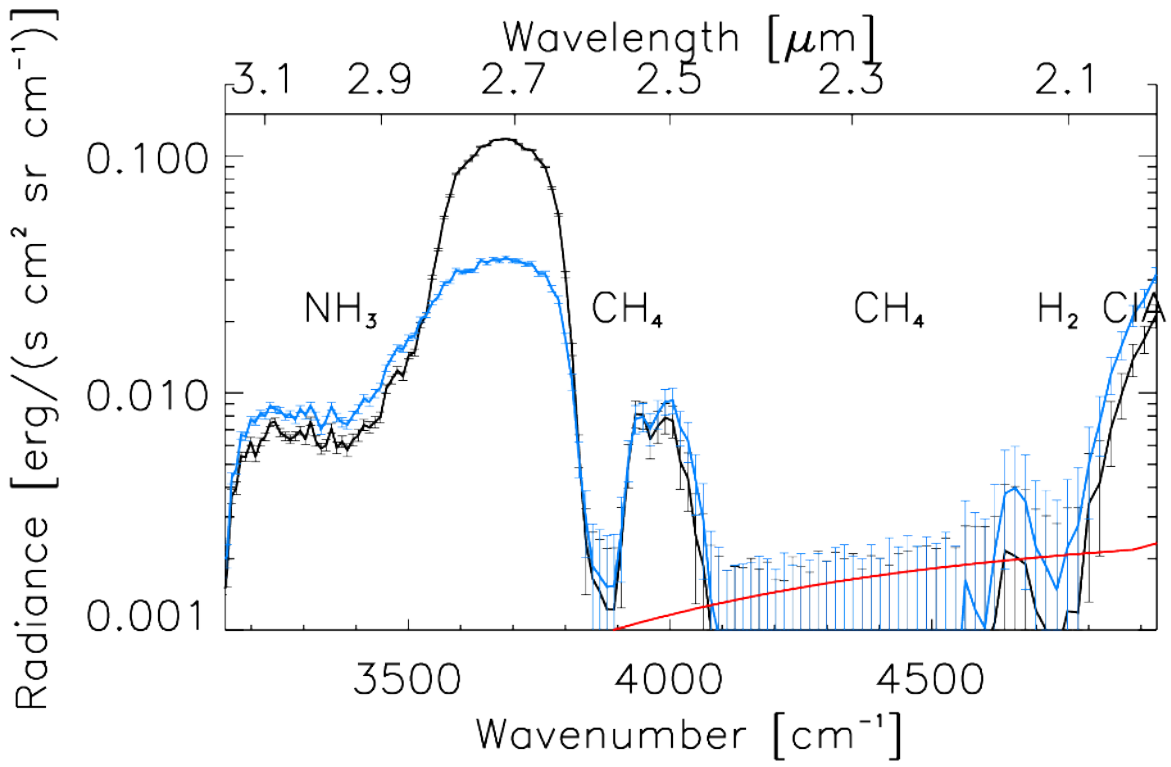

Fig. 2. Two examples of JIRAM spectra of sunlight reflected by the Jupiter's atmosphere. The black curve is a spectrum of relatively high intensity from the South Tropical Zone (28.4°S, 15.4°W). The blue curve is a spectrum of low intensity from the Great Red Spot wake (15.3°S, 323.1°W). The red curve shows the noise equivalent radiance (NER), as estimated from standard deviation of deep-space observations.

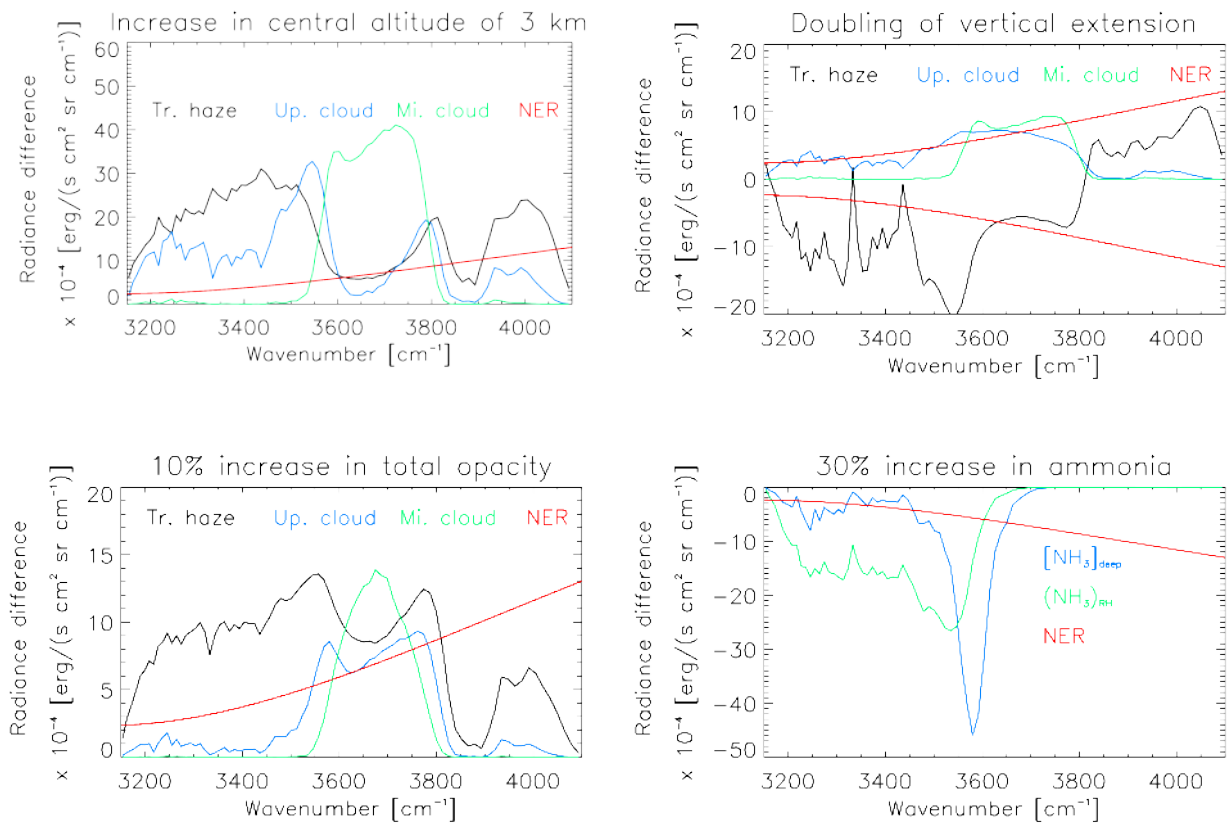

Figure 3. Spectral variations corresponding to realistic variations of fit parameters. Most parameters are defined as strictly positive; to ensure that code does not return non-physical values, we consider during retrieval their logarithms instead than actual values (see table S4 in supplemental materials for further details).

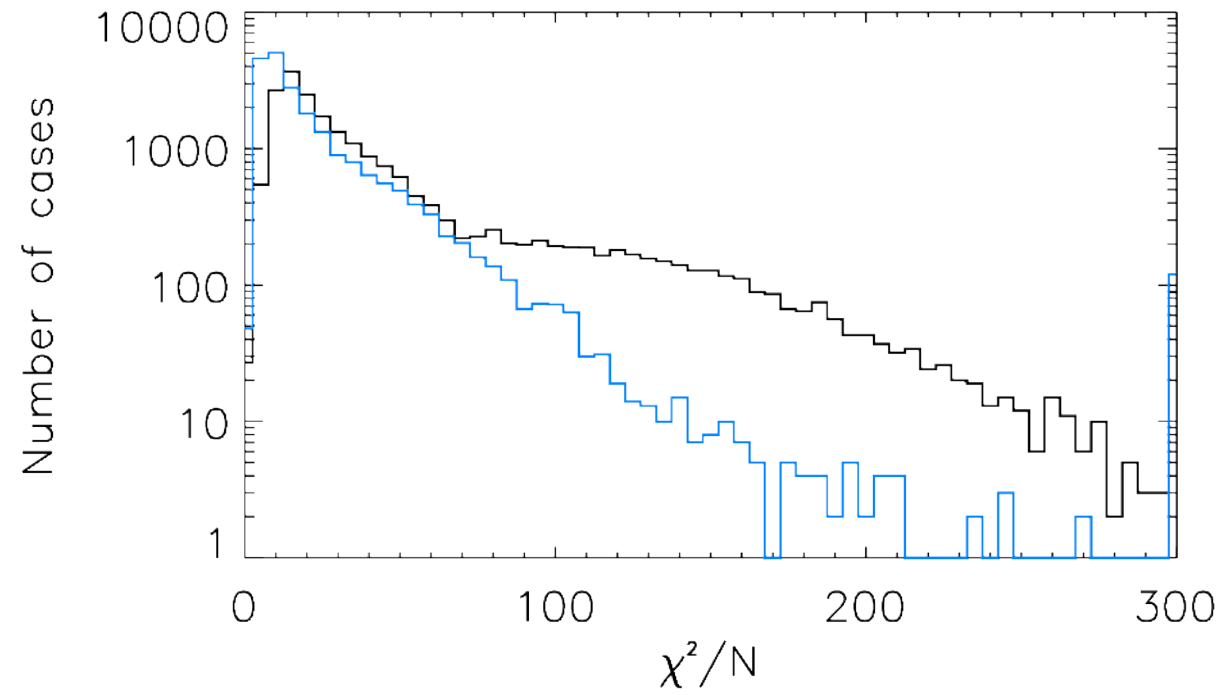

a

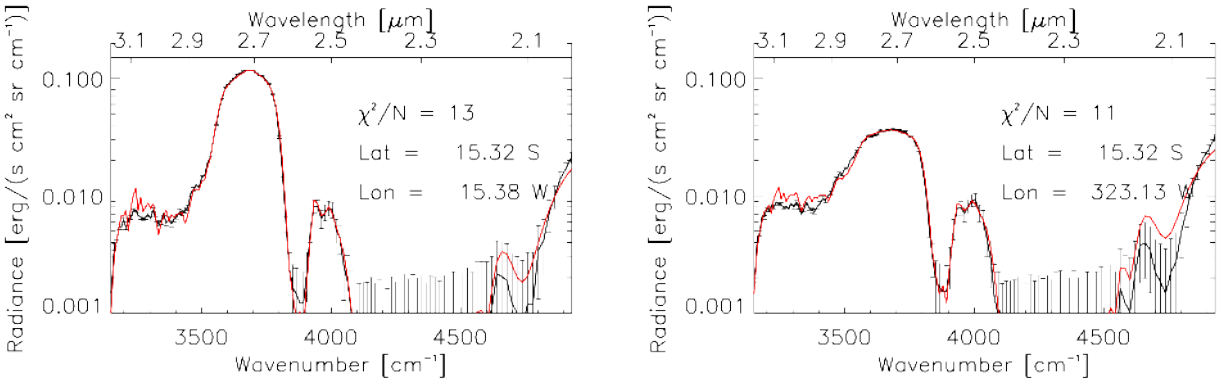

b c

Figure 4: Fit quality achieved by the retrieval code.
Panel a. shows the distribution of χ^2/N values for the data presented in Fig. 1. Bin size is equal to 5; last bin cumulates all the cases with $\chi^2 > 300$. Black curves refers to χ^2/N as computed over the entire spectral range considered during retrieval. Blue curve refers to χ^2/N as computed over the spectral range 3350-4100 cm^{-1}.
Panels b. and c. show the best-fit spectra (in red) for the example data of Fig. 2 (in black). Error bars for JIRAM data equals to the NER value presented in Fig. 2.

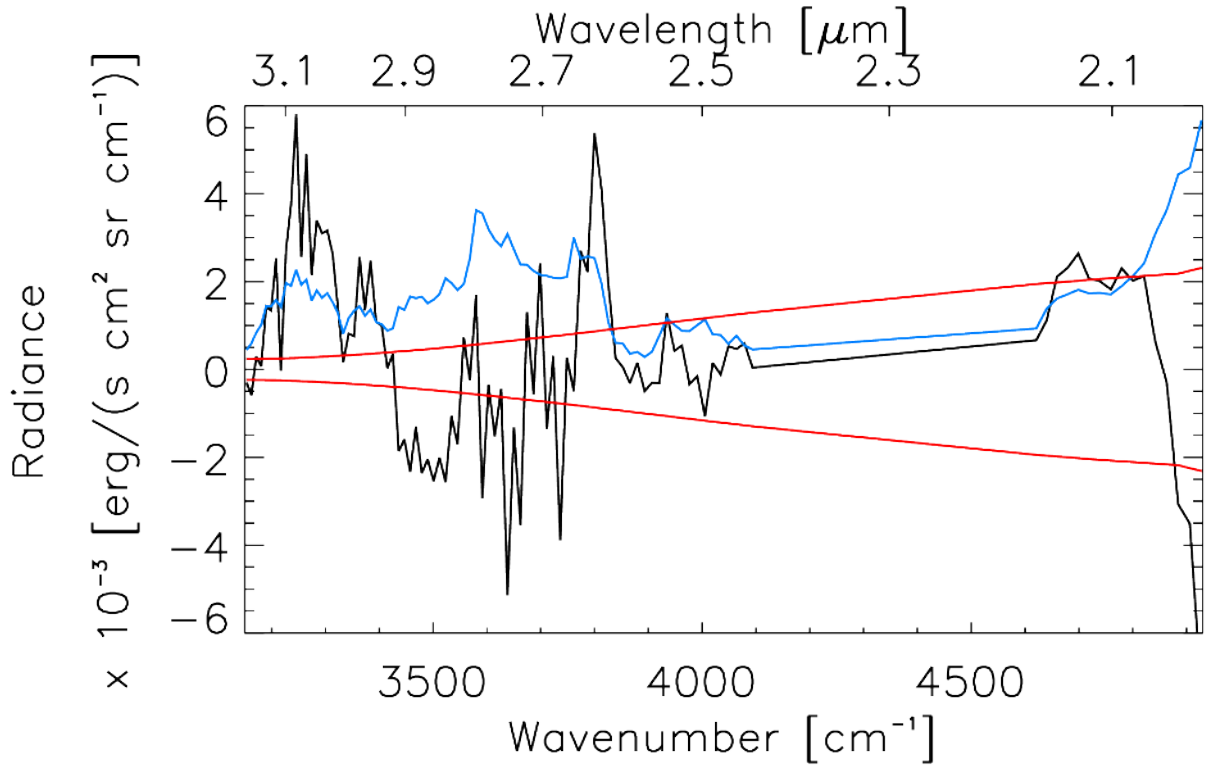

Figure 5. Mean (black curve) and standard deviation (blue) of the residual for cases with $\chi^2/N <$ 200, compared to NER (red curve).

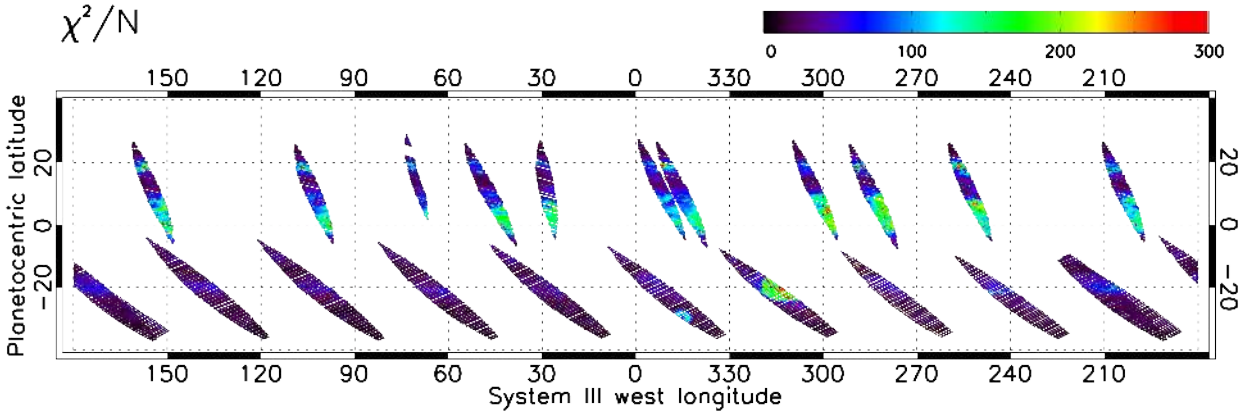

a

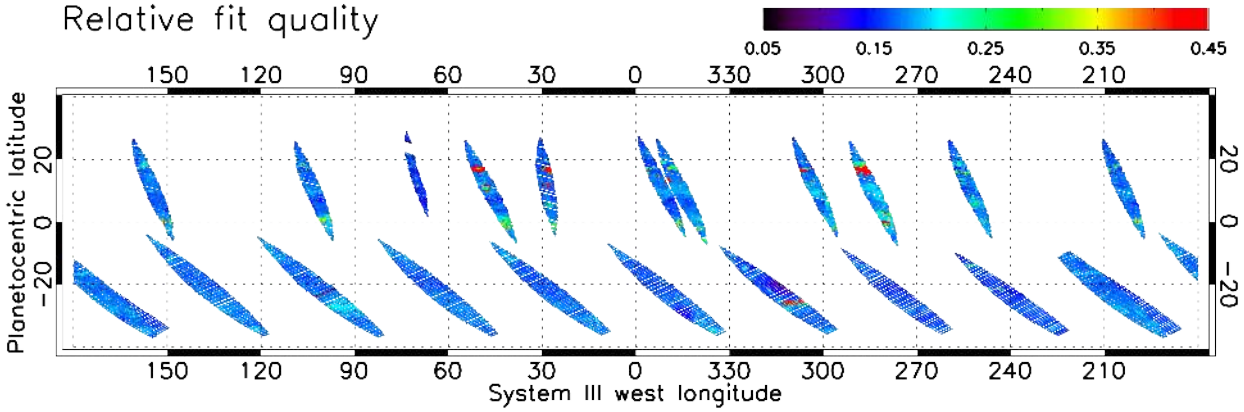

b

Figure 6. Quality of fit, computed in the spectral ranges [3150-4100] and [4610-4930] cm^{-1}.
Panel a: as defined by χ^2/N.
Panel b: as defined by relative fit quality parameter (eq. 1 of Grassi et al. [2020]).
The latter gives the mean relative discrepancy between observed and best fit spectrum over the spectral interval. Higher values imply poorer fit.

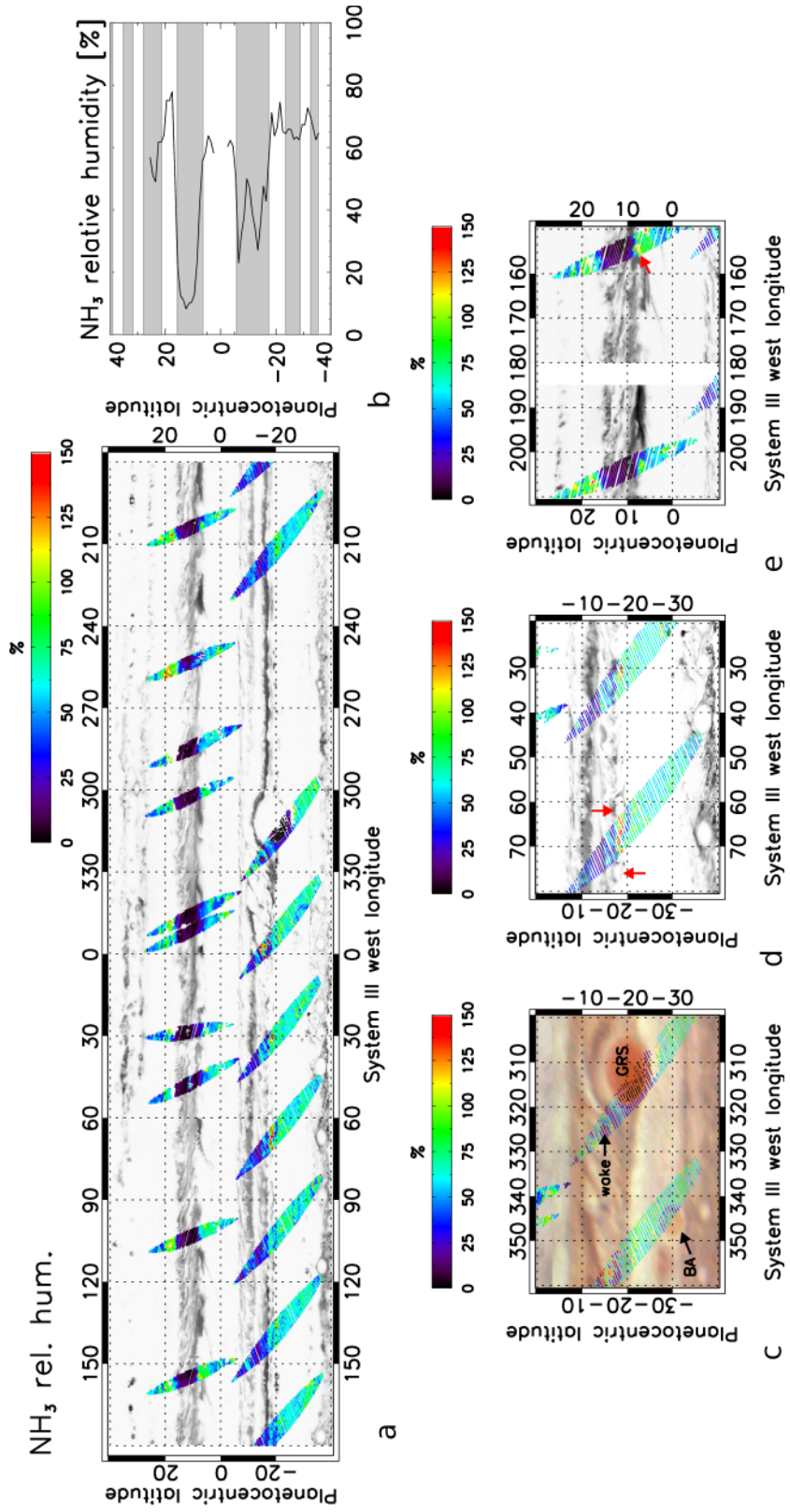

Fig. 7. Relative humidity of ammonia at 500 mbar, as inferred from JIRAM spectral data acquired during PJ1 passage. Panel a: global distribution. Panel b: latitudinal average (i.e.: mean over different longitudes once data have been classified in bins 1°-wide in latitude). Panels c, d, e: details from panel a. in different regions. Background images are from JIRAM M-filter data (black and white) or JunoCam mosaic (in color). Both JIRAM M-filter and JunoCam data have *not* been acquired simultaneously to overlying JIRAM spectral data and some shifts in latitude may exists because of zonal winds. Shades in Panel b. provide indicative positions of belts and zones. Arrows in panels c, d, and e points to different details described in the text.

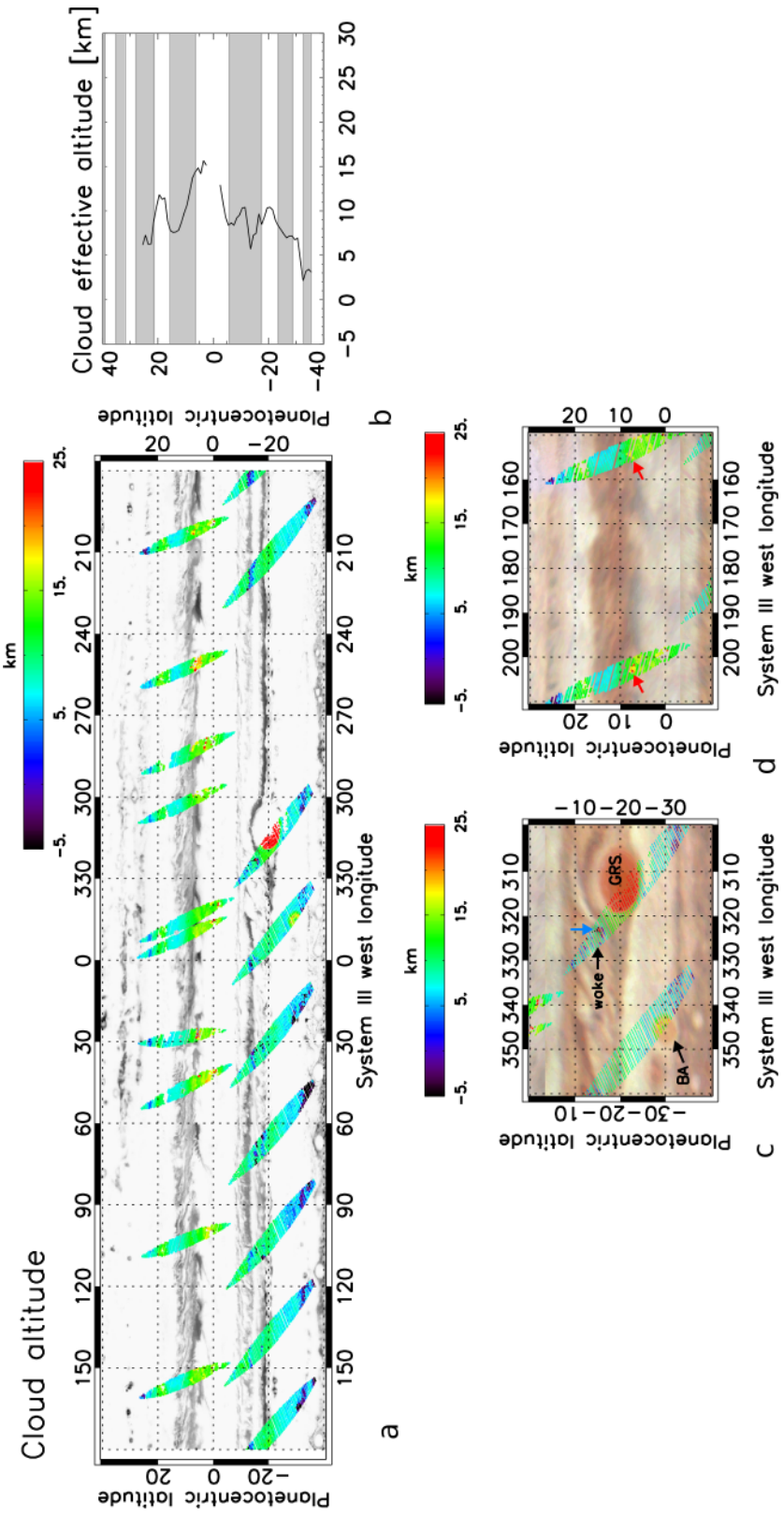

Fig. 8. As figure 7, but for effective cloud altitude in reference to the 1 bar surface (see Section 3 for the definition of this parameter). Note that magnified areas are not the same in the two figures.

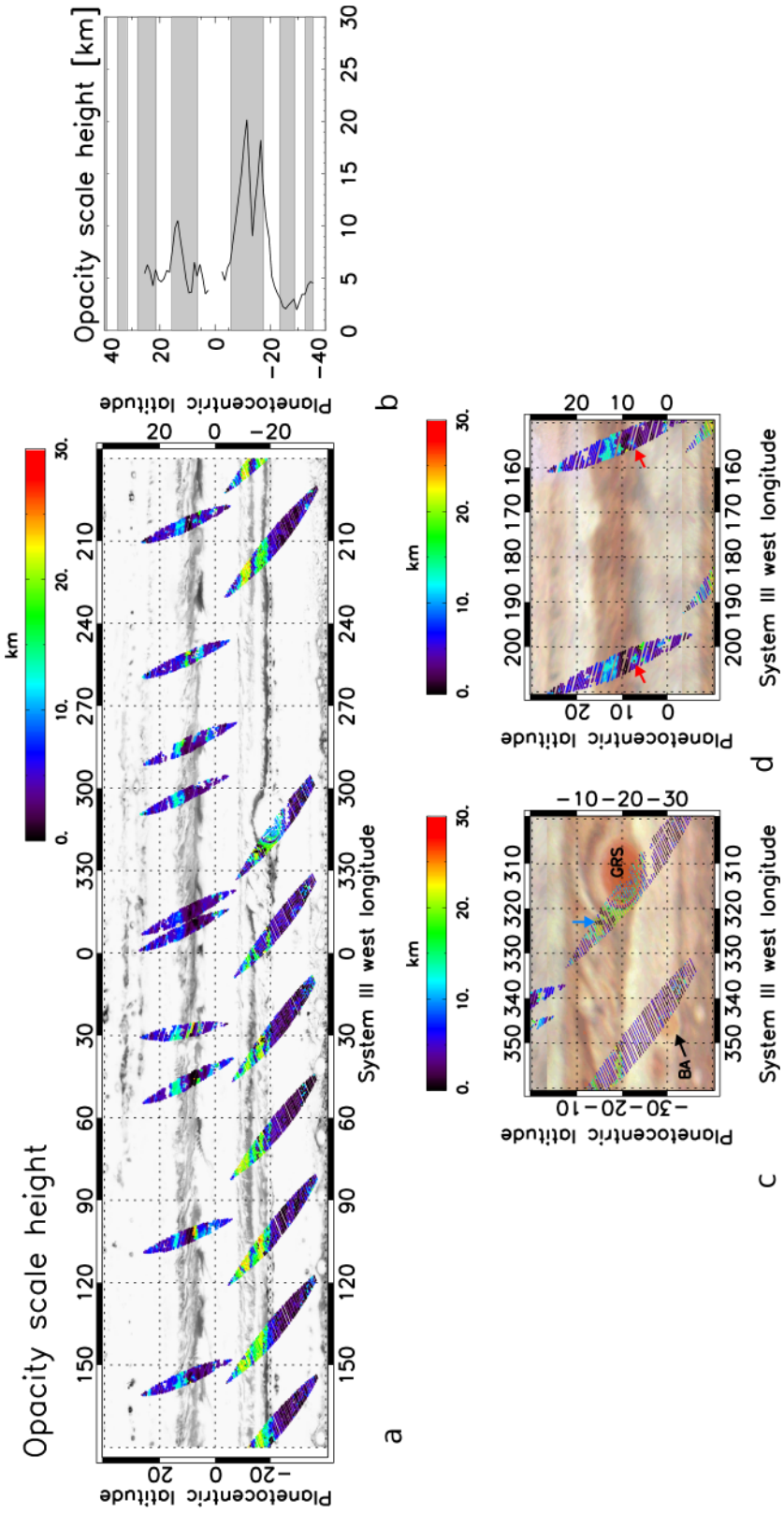

Fig. 9. As figure 7, but for opacity scale height (see Section 3 for the definition of this parameter). Note that magnified areas are not the same in the two figures.

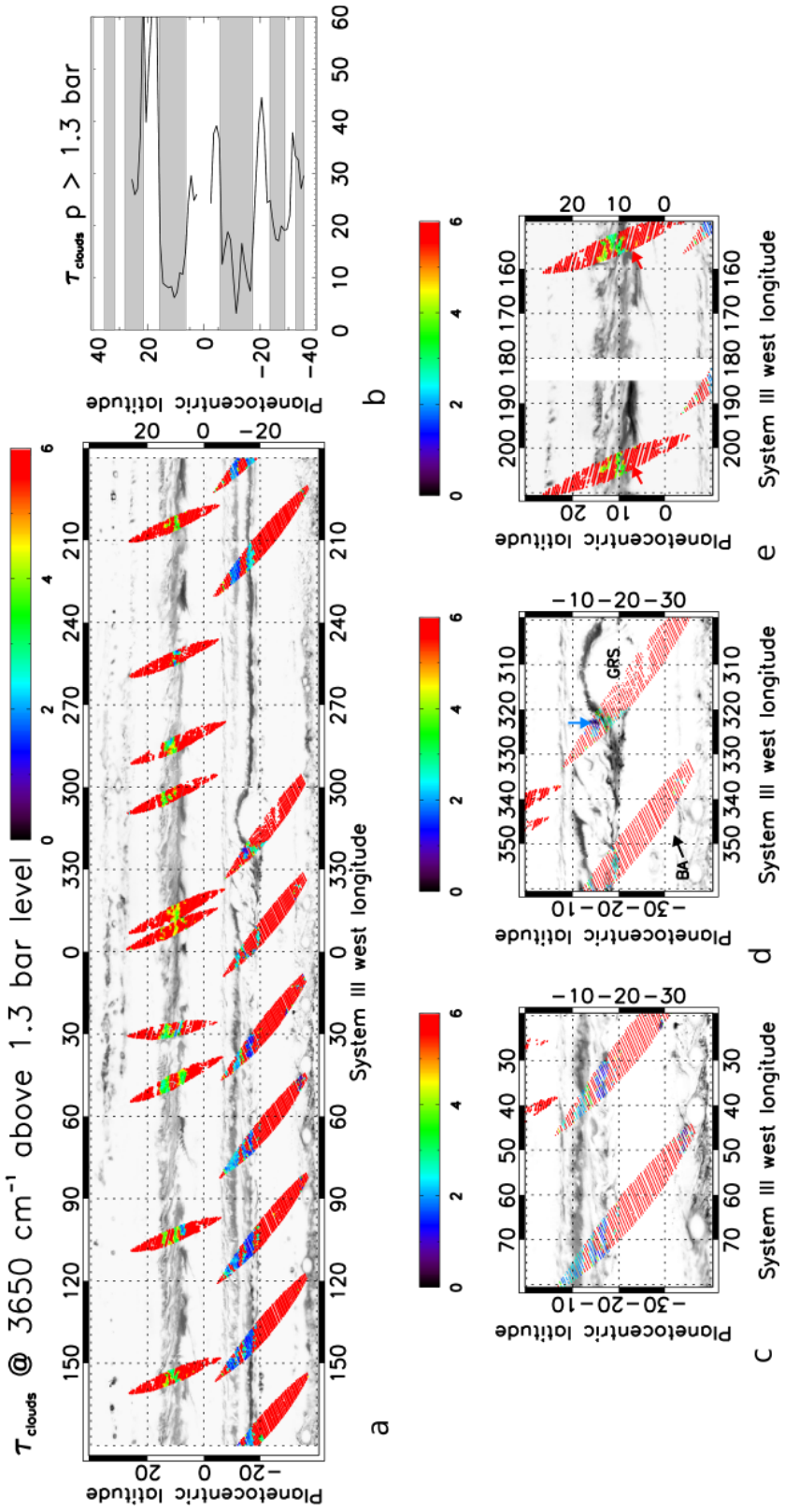

Fig. 10. As figure 7, but for total aerosol optical thickness at 3650 cm^{-1} for altitudes above the 1.3-bar level. Note that magnified areas are not the same in the two figures.
Color code of Fig. 10a is strongly compressed toward high values, to provide better visibility of low-opacity regions. Noteworthy, most regions presented in red have indeed opacity values much higher than the upper limit of color bar and contribute substantially to the high latitudinal average values presented in Fig. 10b

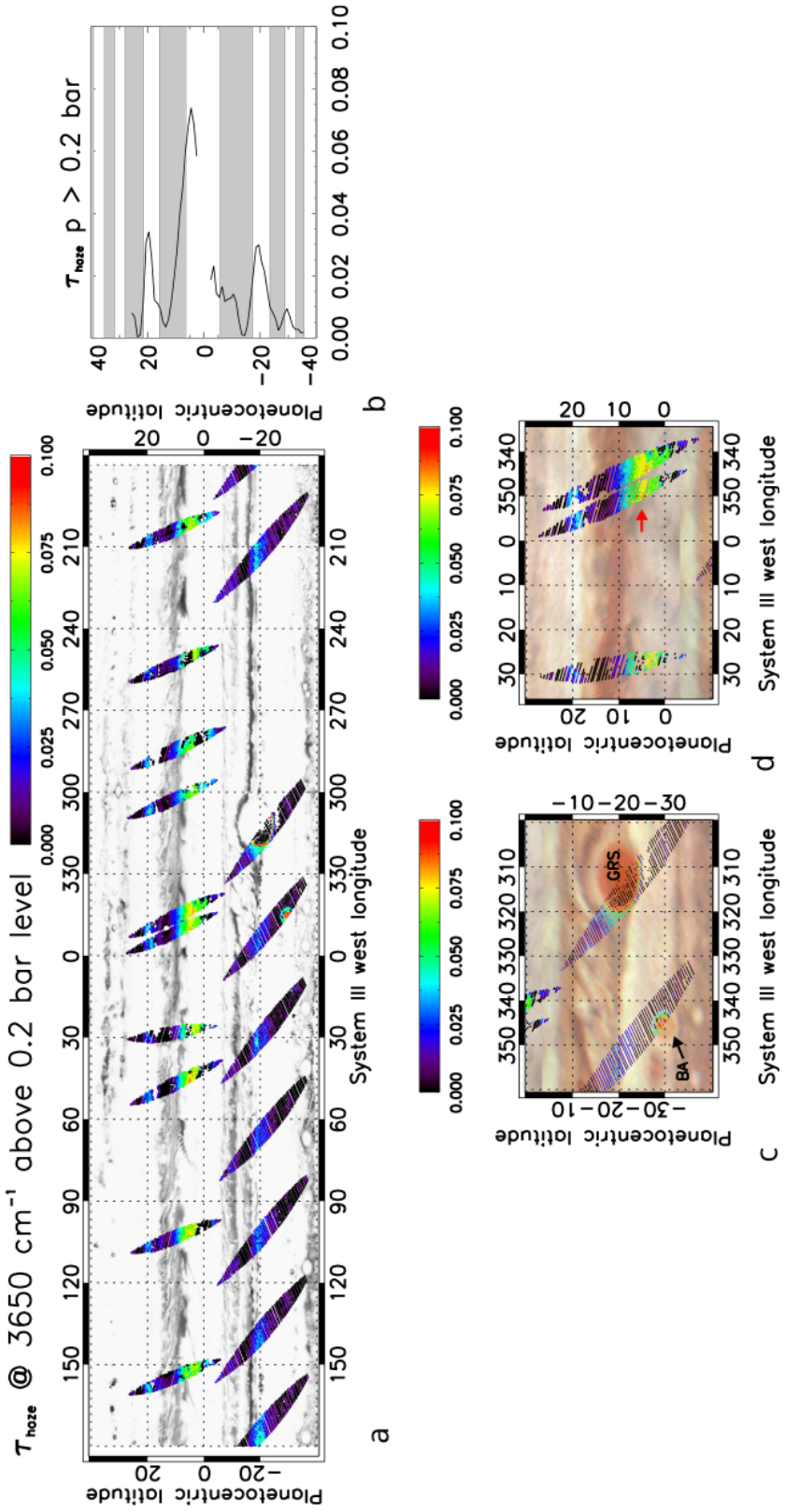

Fig. 11. As figure 7, but for total haze optical thickness at 3650 cm^{-1} for altitudes above the 0.2-bar level. Note that magnified areas are not the same in the two figures.

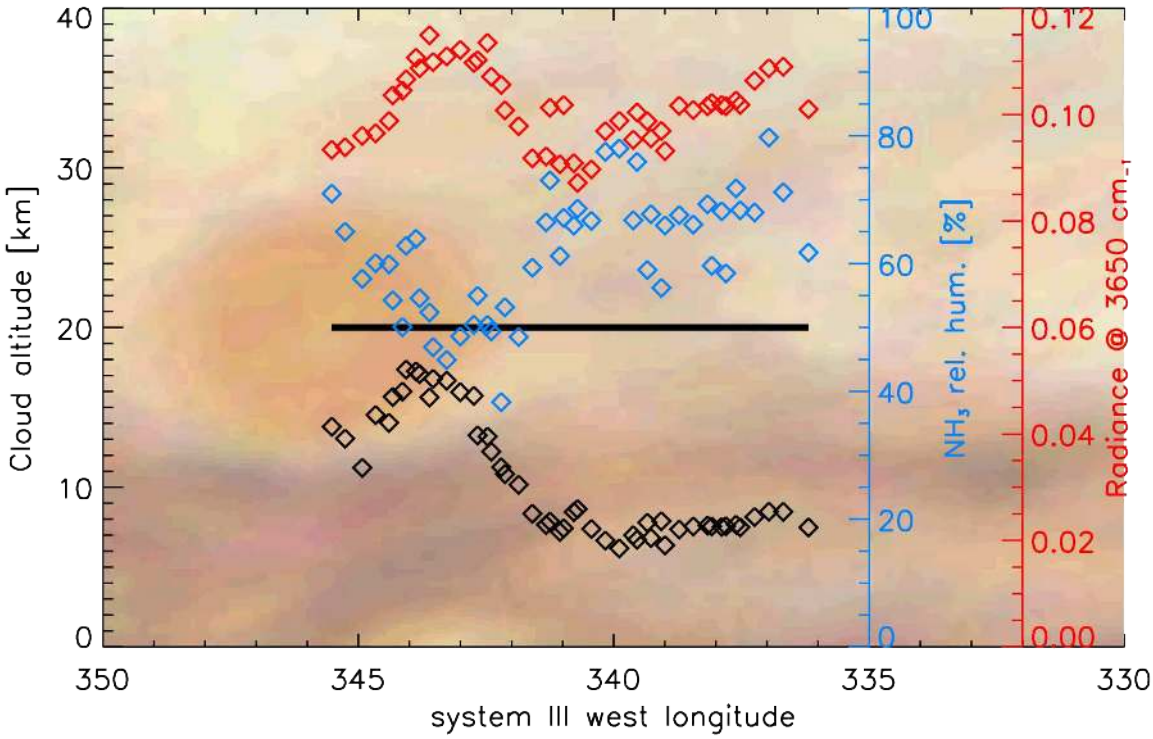

Fig. 12. Longitudinal trends of: cloud altitude (black diamonds), ammonia relative humidity (blue) and signal measured by JIRAM at 3650 cm^{-1} (red) across the center of oval BA. On the background there is a context image by JunoCam, showing, as a black thick line, the section position. Resolution of JunoCam image is approximately 570 km.